University Paul Sabatier

Un joli titre

Flaurent HEULLY–ALARY

September 28, 2025

Contents

Chapter 1

Introduction

Chapter 2

Theory and Methodology

2.1 Model Hamiltonian

2.1.1 Spin Hamiltonian

Heiseinberg Hamiltonian

The most well-know Spin Hamiltonian used to describe the magnetic interaction between a pair of spins located on different magnetic centres is the Heiseinberg-Dirac-Van Vleck (HDVV) Hamiltonina, written as:

$$\hat{H}_{HDVV} = -\sum_{i,j} J_{ij} \hat{\mathbf{S}}_i \cdot \hat{\mathbf{S}}_j \tag{2.1.1}$$

where $J_{i,j}$ is the coupling constant, $\hat{\mathbf{S}}_i$ and $\hat{\mathbf{S}}_j$ are the spin operators working on site i and j. Several conventions exist for this Hamiltonian, with negative sign and/or a factor of 2 in front. The coupling constant J can be either positive or negative depending on the magnetic properties of the system, a positive value indicate ferromagnetism with magnetic moment aligned while negative indicate antiferromagnetism with opposite alignement of magnetic moments. This Hamiltonian is regarded as a Spin Hamiltonian as it only invoke the spin degree of freedom of the system and is still to this day used in the description of the isotropic magnetic properties.

The J constant is defined as an effective integral as it involves several mechanisms:

1- Direct exchange originating from the exchange integral K.

2- Indirect exchange involving ionic determinants.

3- Super-exchange where a diamagnetic bridging ligand open new pathway for exchange mechanisms.

The origins and contributions of these mechanisms to the effective integral can be understood from the Hubbard Hamiltonian in the case of two electrons in two orbitals. Up to the second order perturbation theory, the following expression can be obtained for the effective integral J:

$$J = 2K - \frac{4t^2}{U} \tag{2.1.2}$$

where K is the exchange integral which is always positive, t the hopping integral between the two unpaired electrons and U the on site Coulomb repulsion. This expression shows the competition between a ferromagnetic component (direct exchange $K>0$) and an

antiferromagnetic one (indirect exchange). The contribution of super-exchange cannot be estimated at second-order and requires going up to fourth-order pertubation giving a similar expression:

$$J = 2K - \frac{4t_{eff}^2}{U} \tag{2.1.3}$$

where t_{eff} is now an effective hopping integral involving the bridging ligand, the hopping term between metal and ligand being much larger than the metal to metal one, the t term is usually neglected in this expression. Note that the perturbation expansion is valid only in case of $U >> t$, when the system's behavior is not dominated by delocalisation that would render the HDVV Hamiltonian inadecate.

Ising Hamiltonian

The eigenfunctions of the Heiseinberg Hamiltonian are eigenfunctions of the $\hat{\mathbf{S}}^2$ operator, making them mostly multi-determinental functions which can only be obtained via specific computational methods. To draw an easier picture, it is possible to restrict the spin vector to its component along the z axis alone essentially reducing this to a classical spin problem.

$$H_{ising} = -\sum_{i,j} J_{ij} \hat{\mathbf{S}}_{z,i} \hat{\mathbf{S}}_{z,j} \tag{2.1.4}$$

The magnetic moment of each magnetic site are now considered to align themselves with the z axis at all time, taking a ± 1 value. The main advantage of this approximation is that the eigenfunctions of this Hamiltonian are now spin functions opening up the extraction to new computation methods. It also reduces the analytical derivation allowing to work on larger systems without the need to diagonalize large matrices.

2.1.2 Magnetic anisotropy in mononuclear complexes

Effects such as Spin-Orbit-Coupling (SOC) tend to create anisotropy in systems that cannot be described only by eq (2.1.1). More specifically on mononuclear systems (only one magnetic centre) with a ground state of spin larger or equal to one and correct symmetry conditions, a lift of degeneracy between the different M_S component of a same S state can be observed even in the absence of magnetic field, this phenomenon is called Zero-Field-Splitting.

The associated spin Hamiltonian is written:

$$\hat{H}_{ZFS} = \hat{\mathbf{S}} \cdot \overline{\overline{D}} \cdot \hat{\mathbf{S}} \tag{2.1.5}$$

where $\hat{\mathbf{S}}$ is the spin vector of the ground state and $\overline{\overline{D}}$ is a two rank symmetric tensor. In an arbitrary axis frame, it is composed of six different parameters.

$$\overline{\overline{D}} = \begin{pmatrix} D_{xx} & D_{xy} & D_{xz} \\ D_{xy} & D_{yy} & D_{yz} \\ D_{xz} & D_{yz} & D_{zz} \end{pmatrix} \tag{2.1.6}$$

This tensor can be reduced to three parameters by diagonalization, *i.e* expressing them in the tensor principal axes that define the magnetic anisotropy axes. Going further as to work with traceless tensors allow us to use only two parameters, by convention the z-axis is taken as the main magnetic axis with D the axial parameter:

$$D = D_{zz} - \frac{1}{2}(D_{xx} + D_{yy}) = \frac{3}{2} D_{zz} \tag{2.1.7}$$

and the rhombic term:

$$E = \frac{1}{2}(D_{xx} - D_{yy}) \tag{2.1.8}$$

With $|D| \geq 3E \geq 0$. The ZFS Hamiltonian can then be written:

$$\hat{H}_{ZFS} = D(\hat{S}_z^2 - \frac{1}{3}\hat{S}^2) + E(\hat{S}_x^2 - \hat{S}_y^2) \tag{2.1.9}$$

A positive value of D indicates that the ground state is mainly composed of the M_S=0 component meaning that the projection of the spin moment along the z-axis is close to zero resulting in an easy-plane anisotropy. On the contrary if D<0, the ground state is formed from the M_S=$\pm M_{Smax}$ components with a maximum projection of spin moment along the z-axis resulting in an easy-axis anisotropy.

In the case of a triplet S=1 ground stat such as a nickel Ni (II) complex, the matrix representation of hamiltonian (2.1.5) in an arbitrary axes frame:

H_{ZFS}	$\|1,-1\rangle$	$\|1,0\rangle$	$\|1,1\rangle$
$\langle 1,-1\|$	$\frac{1}{2}(D_{xx} - D_{yy}) + D_{zz}$	$-\frac{\sqrt{2}}{2}(D_{xz+iD_{yz}})$	$\frac{1}{2}(D_{xx} - D_{yy} + 2iD_{xy})$
$\langle 1,0\|$	$-\frac{\sqrt{2}}{2}(D_{xz-iD_{yz}})$	$D_{xx} + D_{yy}$	$\frac{\sqrt{2}}{2}(D_{xz} + iD_{yz})$
$\langle 1,1\|$	$\frac{1}{2}(D_{xx} - D_{yy} - 2iD_{xy})$	$\frac{\sqrt{2}}{2}(D_{xz} - iD_{yz})$	$\frac{1}{2}(D_{xx} + D_{yy}) + D_{zz}$

In the magnetic axes frame, this matrix becomes:

H_{ZFS}	$\|1,-1\rangle$	$\|1,0\rangle$	$\|1,1\rangle$
$\langle 1,-1\|$	$\frac{1}{2}(D_{XX} + D_{YY}) + D_{ZZ}$	0	$\frac{1}{2}(D_{XX} - D_{YY})$
$\langle 1,0\|$	0	$D_{XX} + D_{YY}$	0
$\langle 1,1\|$	$\frac{1}{2}(D_{XX} - D_{YY})$	0	$\frac{1}{2}(D_{XX} + D_{YY}) + D_{ZZ}$

Removing the trace from the tensor and applying the convention from eq(2.1.7) and eq(2.1.8) we get:

H_{ZFS}	$\|1,-1\rangle$	$\|1,0\rangle$	$\|1,1\rangle$
$\langle 1,-1\|$	$\frac{1}{3}D$	0	E
$\langle 1,0\|$	0	$\frac{2}{3}D$	0
$\langle 1,1\|$	E	0	$\frac{1}{3}D$

Note that in the case of an even number of unpaired electrons, the D and E parameters can be estimated directly from the energy spectrum. In the case of a triplet ground state, diagonalizing the model Hamiltonian matrix gives the three eigenvalues:

$$E_1 = -\frac{2}{3}D \tag{2.1.10}$$

$$E_2 = \frac{1}{3}D + E \tag{2.1.11}$$

$$E_3 = \frac{1}{3}D - E \tag{2.1.12}$$

with the eigenvectors:

$$\psi_1 = |1,0\rangle \tag{2.1.13}$$

$$\psi_2 = \frac{1}{\sqrt{2}}(|1,-1\rangle + |1,1\rangle) \tag{2.1.14}$$

$$\psi_3 = \frac{1}{\sqrt{2}}(|1,-1\rangle - |1,1\rangle) \tag{2.1.15}$$

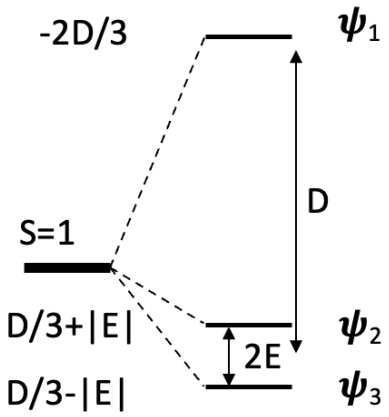

Figure 2.1: Schematic representation of the three lowest SO-state undergoing ZFS in the case of triplet ground state.

leading to the extraction of the D and E terms directly from the energies:

$$D = \frac{1}{2}(E_2 + E_3) - E_1 \tag{2.1.16}$$

and

$$E = \frac{1}{2}(E_2 - E_3) \tag{2.1.17}$$

For the study of system with a ground state of $S < 2$ these two parameters are enough to reproduce accurately the energy spectrum. In case of larger $S \geq 2$, one needs to introduce the Stevens operators which are linked to the crystal field and can be expressed from angular momenta operators $\hat{J}$ These operators were first derived to describe the lift of degeneracy induced by the crystal field potential studied in spectroscopy. Note that this formalism is not resticted to transition metals but is also used for rare earth complexes. The ZFS is now described by a more complete model Hamiltonian:

$$\hat{H}_{Stevens} = \sum_{k=0}^{2S} \sum_{n=0}^{k} B_k^n \hat{O}_k^n \tag{2.1.18}$$

where B_k^n are the Stevens parameter specific to each systems and $\hat{O}_k^n$ the Stevens Operators are spherical tensors of rank k. In case of mono-nuclear complexes, only the even rank k tensors contribute for symmetry reasons. The ZFS parameters are related to the second rank Stevens parameters:

$$D = 3B_2^0 \qquad\qquad E = B_2^2 \tag{2.1.19}$$

2.1.3 Magnetic anisotropy in polynuclear complexes

Opening the study to multiple magnetic centers introduces couplings that can be anisotropic between the magnetic moments of each center. This coupling between two

sites A and B with at least one magnetic electron each, is called anisotropic exchange interaction and is described by the following Giant Spin Hamiltonian.

$$\hat{H}_{AB} = \hat{\mathbf{S}}_A \cdot \overline{\overline{D}} \cdot \hat{\mathbf{S}}_B \tag{2.1.20}$$

The interaction tensor $\overline{\overline{D}}$ describes Zero-Field-Splitting the same way as before but now between two sites A and B, two parameters D and E can be defined similarly. This Hamiltonian is suiTable for system with a ground state of spin larger or equal to one that is well separated in energy from other SO-states. This tensor can be split in three components, an isotropic term that relates to the HDvV Hamiltonian and two anisotropic terms. It is then possible to study all the states of the configuration using the multi-spin Hamiltonian:

$$\hat{H}_{AB} = J(\hat{\mathbf{S}}_A \cdot \hat{\mathbf{S}}_B) + \hat{\mathbf{S}}_A \cdot \overline{\overline{D}}_{AB} \cdot \hat{\mathbf{S}}_B + \mathbf{d}_{AB} \cdot (\hat{\mathbf{S}}_A \times \hat{\mathbf{S}}_B) \tag{2.1.21}$$

where J is the isotropic coupling constant found in the HDvV Hamiltonian 2.1.1. The two following terms describe the anisotropic exchange with the symmetric tensor of exchange $\overline{\overline{D}}_{AB}$ and the antisymmetric exchange $\mathbf{d}_{AB}$ also called Dzyaloshinskii-Moriya pseudo-vector interaction. For couplings involving more than one unpaired electron per site, local tensor must be introduced:

$$\hat{H}_{AB} = J(\hat{\mathbf{S}}_A \cdot \hat{\mathbf{S}}_B) + \hat{\mathbf{S}}_A \cdot \overline{\overline{D}}_{AB} \cdot \hat{\mathbf{S}}_B + \mathbf{d}_{AB} \cdot (\hat{\mathbf{S}}_A \times \hat{\mathbf{S}}_B) + \hat{\mathbf{S}}_A \cdot \overline{\overline{D}}_A \cdot \hat{\mathbf{S}}_A + \hat{\mathbf{S}}_B \cdot \overline{\overline{D}}_B \cdot \hat{\mathbf{S}}_B \tag{2.1.22}$$

The matrix representation for two interacting spin $1/2$ systems is the following:

H_{MS}	$\lvert 1,-1\rangle$	$\lvert 1,0\rangle$	$\lvert 1,1\rangle$	$\lvert 0,0\rangle$
$\langle 1,-1\rvert$	$\frac{J}{4} + \frac{D_{zz}}{4}$	$\frac{D_{xz}-iD_{yz}}{2\sqrt{2}}$	$\frac{(D_{xx}-D_{zz}-2iD_{xy})}{4}$	$\frac{d_y+id_x}{2\sqrt{2}}$
$\langle 1,0\rvert$	$\frac{D_{xz}+iD_{yz}}{2\sqrt{2}}$	$\frac{J}{4} - \frac{D_{zz}}{4} + \frac{(D_{xx}+D_{yy})}{4}$	$-\frac{D_{xz}-iD_{yz}}{2\sqrt{2}}$	$-\frac{id_z}{2}$
$\langle 1,1\rvert$	$\frac{(D_{xx}-D_{zz}+2iD_{xy})}{4}$	$-\frac{D_{xz}+iD_{yz}}{2\sqrt{2}}$	$\frac{J}{4} + \frac{D_{zz}}{4}$	$\frac{d_y-id_x}{2\sqrt{2}}$
$\langle 0,0\rvert$	$\frac{d_y-id_x}{2\sqrt{2}}$	$\frac{id_z}{2}$	$\frac{d_y+id_x}{2\sqrt{2}}$	$-\frac{3J}{4} - \frac{D_{zz}}{4} - \frac{(D_{xx}+D_{yy})}{4}$

From this matrix, we notice that the Dzyaloshinskii-Moriya interaction creates a coupling between the singlet with the three M_S components of the triplet state. As for the symmetric tensor of anisotropic exchange, it only couples the three component of the triplet which undergo an energy splitting. At the isotropic level, the difference between the triplet and singlet states is given by $\Delta E = J$, but with the inclusion of the anisotropic terms this becomes much more complex. As opposed to the Zero-Field Splitting mechanism, it is impossible to obtain values for these interactions from the energy spectrum only, as such they will be extraced from the effective Hamiltonian theory. Note that this Hamiltonian 2.1.22 is not restricted to a ground state with $S \geq 1$.

2.2 Methodology

All types of calculations discussed here after have for purpose to solve, in some way, the Schrodinger Equation:

$$\hat{H}\Psi_i = E_i\Psi_i \tag{2.2.1}$$

where $\hat{H}$ is an Hamiltonian used to describe the system, E_i is the energy associated to the wave-function Ψ_i. The solutions E_i of this problem are obtained pretty straightforwardly by diagonalizing the Hamiltonian matrix, except that in most cases, the Ψ_i vector are not known beforehand. The Hamiltonian treated during the calculations is called exact electronic Hamiltonian as it considers all electronic and nuclear interactions of the system, it is written as follow, in atomic units:

$$\hat{H} = -\frac{1}{2}\sum_{i=1}^{N}\nabla_i^2 - \sum_{A=1}^{M}\frac{1}{2M_A}\nabla_A^2 - \sum_{i=1}^{N}\sum_{A=1}^{M}\frac{Z_A}{|r_i - R_A|} + \sum_{i=1}^{N}\sum_{j<i}^{N}\frac{1}{r_{ij}} + \sum_{A=1}^{M}\sum_{B>A}^{M}\frac{Z_A Z_B}{|R_A - R_B|} \tag{2.2.2}$$

where r_i is the position vector of the ith electron, R_A the position vector of the Ath nucleus with atomic number Z_A and mass M_A. This Hamiltonian can be simplified in the context of the Born-Oppenheimer approximation, the electrons are considered to adapt instantly to the movement of the nuclei. This allows to decouple the movement of the electrons from that of the nuclei, whose position can be fixed at the equilibrium (or any other geometry). Note that once the electronic energies and wave-funcion have been obtained for different geometries, it is also possibe to study the nuclei motion within this approximation. This approximation is justified with the fact that the electrons are much lighter than the nuclei.

$$\hat{H}_{elec} = -\frac{1}{2}\sum_{i=1}^{N}\nabla_i^2 - \sum_{i=1}^{N}\sum_{A=1}^{M}\frac{Z_A}{|r_i - R_A|} + \sum_{i=1}^{N}\sum_{j<i}^{N}\frac{1}{|r_i - r_j|} \tag{2.2.3}$$

This Hamiltonian describes the electronic problem while the nuclei contribution, last term from eq 2.2.2 is a constant, having for only effect a shift in the overall energy spectrum. While this greatly simplifies the equations, it is still not solvable analytically and several approximations were developped to tackle this problem. One common point to all the methods that were used in this work relies on the construction of molecular orbitals (**MO**) as expansions of atomic orbitals (**AO**).

$$\psi_k = \sum_i c_i \phi_i \tag{2.2.4}$$

Where ψ_k is the kth MO built from the AOs ϕ_i with coefficient c_i. This expansion relies on a infinite number of AO but in real case application this is not achievable and will thus be restricted to a finite number of basis functions. As the eletronic Hamiltonian does not include any information about spin, it will be included within a so called spin orbital with the introduction of two orthonormal functions $\alpha(\omega)$ and $\beta(\omega)$, *i.e* spin up or down function, with ω a dummy variable. From each spatial molecular orbital, two spin orbitals can be created such that:

$$\chi_i = \begin{cases} \psi_i(r)\alpha(\omega) \\ \quad or \\ \psi_i(r)\beta(\omega) \end{cases} \tag{2.2.5}$$

This definition for the spin orbital is well adapted for close-shell systems where all molecular orbitals are doubly occupied, the spatial part for any spin orbital is the same for both spin function defining the restricted formalism. A commonly used notation in this formalism is to refer to a spin orbital by its spatial component and indicate the spin

function with an overline, *i.e* $\chi_i = \psi_i(r)\alpha(\omega) = \psi_i(r)$ or $\chi_i = \psi_i(r)\beta(\omega) = \overline{\psi}_i(r)$. Such definition changes when working with open shell system, *i.e* some orbitals are singly occupied necessiting the application of unrestricted formalism.

2.2.1 Hartree-Fock Method

The cornerstone of *ab initio* calculation in quantum chemistry is the Hartree-Fock method which is usually the initial step for computing a first approximation of the wave-function in molecules. It is a variational approach that aims to treat the N-electron problems as problem of N non interacting electrons in the presence of an average potential replicating interactions between them, it is in this sense a mean-field theory. This wave-function is constructed on the optimisation of a single Slater determinant Ψ:

$$|\Psi(x_1, x_2, \ldots, x_N)| = \frac{1}{\sqrt{N!}} \begin{vmatrix} \chi_i(x_1) & \chi_j(x_1) & \cdots & \chi_k(x_1) \\ \chi_i(x_2) & \chi_j(x_2) & \cdots & \chi_k(x_2) \\ \vdots & \vdots & & \vdots \\ \chi_i(x_N) & \chi_j(x_N) & \cdots & \chi_k(x_N) \end{vmatrix} \tag{2.2.6}$$

where χ_i are spin orbitals and the variable $x_i = \{r_i, \omega_i\}$, it involves all combination of all N electrons in all k spin orbitals. We introduce the shorthand notation for such determinant $|\Psi(x_1, x_2, \ldots, x_N)| = |\chi_1(x_1)\chi_2(x_2)\ldots\chi_N(x_N)|$ showing only the diagonal elements of the determinant.

The way to obtain the best adapted Hartree-Fock wave-function,*i.e* the molecular orbitals, comes through the resolution of the Roothan's equation:

$$FC = SC\epsilon \tag{2.2.7}$$

S is the overlap matrix of the basis function, ϵ the matrix of orbital energies and C is the matrix of the trial vector. The Fock operator F is defined as:

$$\hat{F}(i) = \hat{h}(i) + \sum_{j}^{N/2} [2\hat{J}_j(i) - \hat{K}_j(i)] \tag{2.2.8}$$

where $\hat{h}(i)$ is a mono-electronic operator that contains the kinetic energy operator of the ith and the coulomb repulsion with the fixed nuclei. The two operators $\hat{J}_j(i)$ and $\hat{K}_j(i)$ describe the coulomb repulsion and exchange mechanism between the ith electron and the rest. These operator carry a direct dependance on the trial vectors from eq 2.2.7 as such, the Roothan's equation are non-linear and will be solved iteratively following a $Self\ Consistent\ Field$ (SCF) procedure.

2.2.2 Configuration Interaction

2.2.3 Complete Active Space Self Consistent Field

For most of magnetic systems, a single reference wave-function is not enough as the system is usually not closed shell and present one or more unpaired electrons. Hence, its ground state is described by a wave-function composed of several determinants. One of the most used method to introduce multiple references in the wave-function is called $Complete\ Active\ Space\ Self\ Consistent\ Field$ ($CASSCF$). Compared to

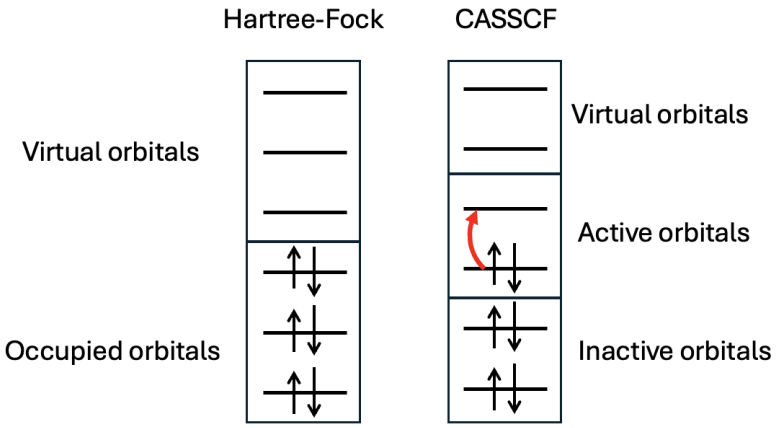

Figure 2.2: Difference between the orbitals space in Hartree-Fock and CASSCF Theory

the Hartree-Fock theory where two types of orbitals (occupied and unoccupied) were considered, in CASSCF theory orbitals are separeted in three sub-spaces. The inactive orbitals are doubly occupied throughout the calculation, virtual orbitals will stay empty while the active orbitals have a variable occupancy ranging from zero to two electrons. These active orbitals define the active space into which a configuration interaction will be realised considering all the possible determinants within this sub-spaces. As the number of determinants grows significally with the number of orbitals included in the active space, this method is quite costly and its size becomes a limiting factor for the calculations. The new wave-function is now written as an expansion of Slater determinants which is obtained via a SCF procedure where both the expansion coefficients and the orbitals are optimised as to minimize the ground state energy or of several states in an "average" way. This dual optimisation scheme can render the convergence troublesome, as such the definition of the active space and the choice of the starting orbitals becomes crucial. One usually starts from a set of orbitals previously obtained via an Hartree-Fock calculation. For computation of magnetic properties in transition metal systems, the minimum active space should consists of the magnetic orbitals, *i.e* the singly occupied d-orbitals of the metallic centers, this can later be extended to all of the 3-d orbitals of the metal as well as some orbitals of the ligands. As a result of the CASSCF method we obtain the energies of all states included in the calculation and a new set of orbitals into which they are expressed. Note that depending on the computational code used, the sets of orbitals may be $specific$ to a single state or $averaged$ to lower the average energy of all of the states computed. This calculation takes into account the correlation between the electrons inside the active space in the mean field created by the other electrons. While this method provides the non-dynamical correlation, it fails to capture the correlation with the inactive electron and their reponse to excitations, called dynamic-correlation and the need to look further appears.

2.2.4 Perturbation Theory

Perturbative treatment can be applied to extract the dynamical correlation brought by the mono and diexcitations that is left out from simple CASSCF calculation. For such calculation, one can use the CASPT (Complete Active Space Perturbation theory) or the NEVPT (N-electron valence state perturbation theory). Both of these methods rely on the assumption that the Hamiltonian can be partitioned into a zeroth-order term and a perturbation with the parameter λ:

$$\hat{H} = \hat{H}^{(0)} + \lambda\hat{H}^{(1)} + \lambda^2\hat{H}^{(2)} + \dots \tag{2.2.9}$$

The wave-function and energy are expanded in a similar way and the zeroth order term $\Psi^0_{(0)}$ is chosen to be the CASSCF wave-function. The effect of the configurations outside of the active space on the energy and the wave-function is estimated though perturbation theory and the expansions of the equations allows one to obtain the corrected energies usually at second order of perturbation with CASPT2 or NEVPT2. These two methods mainly differ from the choise of the zeroth-order Hamiltonian, CASPT2 rely on a monoelectronic Hamiltonian built from a one electron Fock operator that falls back to the Moller-Plesset Hamiltonian in single reference case. This treatment may lead to what is called "intruder states" coming divergence in the denominator of the corrections term where a difference of orbital energy is taken. Several approach have been adapted such as the introduction of *level shifts*, real or imaginary, as to fix this divergence. In case of NEVPT2, the zeroth-order Hamiltonian is a bi-electronic (Dyall) Hamiltoninan which in itself include a shift in energy between state from inside or outside the active space preventing the appearance of intruder states. One should add that the corrections are considered to be contracted as these methods do not act upon the coefficients inside the wave-functions but only on the energies.

2.2.5 Difference dedicated configurational interaction

To get a full picture of the dynamic correlation one has to go to Multi-Referential-Configuration-Interaction (MRCI) methods. This method allows to introduce new determinants in the wave-function that do not belong to the CASSCF space, this way not only the energies but the wave-functions are revised. While very promising this method is not applicable to large systems because of the number of determinants to include in the CI expansion, the cost of calculation becoming too high, one has to truncate the CI space. Restricting the CI to all the simple and double excitations is stil computationally demanding as the double excitation are too numerous, but some of them can be left out of the calculations. These excitations are classified into eight categories depending on the number of hole/particle created represented on Figure 2.3. A hole is an excitation from an inactive orbital to an active or virtual orbital, while a particle is an excitation from an active or inactive orbital to a virtual one.

The most troublesome excitations are the one generating two holes and two particles (2h-2p) as they are the most numerous, but it can be shown that at second order of perturbation they do not contribute to the energy difference between states but only act as a shift of the diagonal energies. As such they can be neglected giving rise to a variant of MRCI called Difference-Dedicated-Configurational-Interaction (DDCI). Three sub-variant of DDCI exists taking into account different classes of excitations as pictured on fig 2.3 It has been established that the extraction of magnetic coupling involving bridging ligand requires the use of the DDCI3 method to provide good estimates.

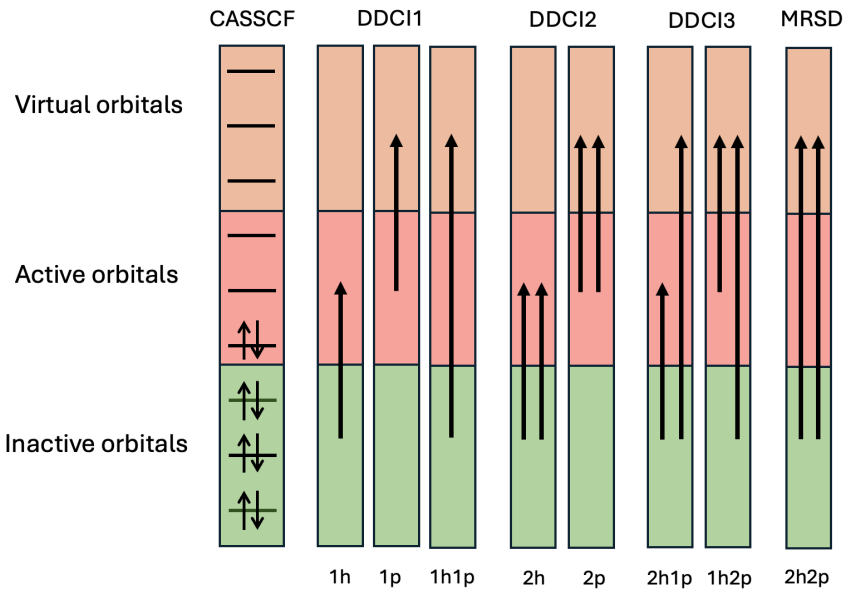

Figure 2.3: Classes of excitations and associated DDCI method

2.2.6 Density functional theory

Another way to get a description of the electronic structure of is through density functional theory (DFT). The main interest of such a method is the description of the ground state properties through the determination of the ground state energy E_0 following the variationl theorem:

$$E_0 = \min \langle \Psi | \hat{H} | \Psi \rangle \tag{2.2.10}$$

Here, the eletronic wave-function of the molcule Ψ is approximated to a single Slater determinant obtained from the determination of the electronic density $\rho(\mathbf{r})$:

$$\rho(\mathbf{r}) = N \int |\Psi(\mathbf{x}_1 \dots \mathbf{x}_N)|^2 ds_1 dx_2 \dots dx_N \tag{2.2.11}$$

The Hamiltonian2.2.2 can be written:

$$\hat{H} = \hat{T} + \hat{V}_{ee} + \hat{V}_{ne} \tag{2.2.12}$$

with $\hat{T}$ the kinetic energy operator, $\hat{V}_{ee}$ the electron-electron interaction operator and $\hat{V}_{ne}$ the nuclei-electron interaction operator. By replacing $v_{ne}(\rho\mathbf{r})$ with a known external potential $v(\mathbf{r})$, one can obtain the ground state wave-function Ψ by solving the Shrodinger equation giving the electron density follows. The first Hohenberg-Kohn theorem states that this external potential is a unique functional of the electron density. As such, knowing the electron density allows to determine the properties of the ground states. The second Hohenberg-Kohn gives in case of non degenerate ground state, the wave-function Ψ is itself a functionl of $\rho(\mathbf{r})$ which allow to define the total energy:

$$E[\rho] = F[\rho] + \int \rho(\mathbf{r}) v(\mathbf{r}) dr \tag{2.2.13}$$

with $F[\rho]$ a universal density functional which contains the kinetic and potential contributions. The ground state energy E_0 is the minimum of eq 2.2.13 which is reached

when the electron density $\rho_0(\mathbf{r})$ is that of the gound state. In theory the knowledge of the electon density allows to determine E_0, however the density dependance expression of $F[\rho]$ is not known.

$$F[\rho] = T[\rho] + V_{ee}[\rho] \tag{2.2.14}$$

Kohn and Sham introduced new definition of this functional by replacing the interacting system with a fictious system of N non interacting electrons.The functional becomes:

$$F[\rho] = T_s[\rho] + J[\rho] + E_{xc}[\rho] \tag{2.2.15}$$

where $T_s[\rho]$ is the non-interacting kinetic energy functional of density ρ expressed in the basis of $\phi_i(\mathbf{r})$ that are built to reproduce the ground state density $\rho(\mathbf{r})$.

$$\rho(\mathbf{r}) = \sum_i^N |\phi_i(\mathbf{r})|^2 \tag{2.2.16}$$

$$T_s[\rho] = \sum_i^n \langle \phi_i | -\frac{1}{2}\nabla^2 | \phi_i \rangle \tag{2.2.17}$$

The Hartree-potential $J[\rho]$ gives the coulomb repulsion between electrons pair:

$$J[\rho] = \frac{1}{2}\int\int \frac{\rho(\mathbf{r}_1)\rho(\mathbf{r}_2)}{|\mathbf{r}_2 - \mathbf{r}_1|} d\mathbf{r}_1 d\mathbf{r}_2 \tag{2.2.18}$$

The energy expression eq 2.2.13 finally becomes:

$$E[\rho] = \int v(\mathbf{r})\rho(\mathbf{r}) d\mathbf{r} + T_s[\rho] + J[\rho] + E_{xc}[\rho] \tag{2.2.19}$$

This definition gives the exact energy given that the expression of the Exchange-Correlation E_{xc} is known, unfortunately this is not the case. Over the years multiple attempts have been made to find a universal expression of E_{xc} in terms of ρ and its derivative. In the most basic approach, called Local Density Approximation (LDA), the system is taken to behave as a uniform electron gas where E_{xc} depends only in the density ρ. This model was later adapted to study different spin configuration with the Local Spin Density Approximation (LSDA). Other attemps tried to improve the functional by incorporating a dependance in the derivative of ρ with the Generalized Gradient Approximation (GGA) or a small portion of the Hartree-Fock exact exchange in what is called hybrid functionals.

2.2.7 Embedded Cluster Method

In the case of molecules, the study of magnetic anisotropy is well described by single molecule calculations as these interactions are localised between the metallic centers and ligands. The restricted size of the molecule generally allows for an explicit treatment of all the atoms involved. The same cannot be said about cristalline systems which are infinite and cannot be treated that way by the methods chosen in this work, as such we have to work on smaller part called "cluster" or "fragment". In theory one would want the fragment to be as large as possible to reduce the error created by cutting off the fragment from its environment, unfortunately to reduce computational cost we have to limit ourselves with small sized fragments. It then becomes crucial to chose correctly the fragment based on our knowledge of the physics we want to reproduce. The properties

of the cluster alone differ from the one inside its natural environment. To reproduce it accurately it is immersed inside an embedding. This embedding is composed of point charges that aim to replicate the electrostatic field of the crystal, called Madelung Field, inside the cluster region. To keep the symmetries of the crystal, the point charges are positionned at the lattice site in a sphere of radius R_c. Another problem in selecting

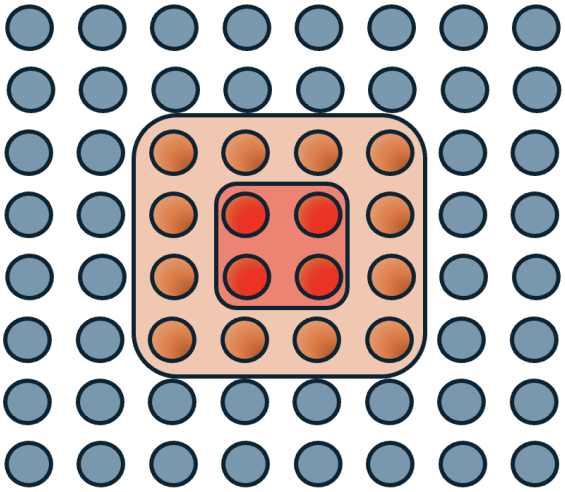

Figure 2.4: Schematic representation of the three region composing the embedding. red: cluster, orange: TIPS, blue: point charges

fragments in ionic crystal is the overall charge of the fragment. The centre of the study is the metallic ions, charged positively, forming ionic bonds with negatively charged ligands. A correct description of these magnetic centres requires to include all closest neighbors which often makes the overall fragment negatively charged. The ions at the border of the fragment, replaced by point charges, are then positive. This induces a polarization of the electron density of the anions bordering the cluster. To avoid the electrons escaping the fragment, pseudo-potentials are placed at the lattice sites near the fragment to act as walls which prevent electrons from approaching these positive charges as if they were real atoms. These potentials are called Total-Ion-Potentials (TIPS) and can be either *ab initio* model potential (AIMP) or Effective Core Potential (ECP) depending on which Quantum Chemistry software is used.

Two procedures were explored to create such embedding:

(1) Formal charges were used in a sphere with very large R_c (around 50 Å).

(2) Optimised point charges were obtained using Ewal Summation from formal charges, this allows to reduce the R_c to a few angstrom around the fragment.

All of this is done to ensure that the properties extracted from the fragment calculations, *i.e* for a finite system, are a good representation of the crystal properties, *i.e* for an infinite system.

2.2.8 Effective Hamiltonian Theory

Having ways to compute the *ab initio* multi-reference wave-functions usually leads to lenghty expression where the wave-function is spanned along a large number of Slater determinant making its analysis complicated. On the other hand, the model

Hamiltonian works in a much smaller space where a small number of electrons is used to introduce effective interactions. A way to connect the two Hamiltonians is to apply a theory developped by Bloch called Effective Hamiltonian theory. Its purpose is to build an effective Hamiltonian whose eigenvalues reproduce the energy spectrum of the *ab initio* Hamiltonian but using a much smaller number of eigenfunctions.

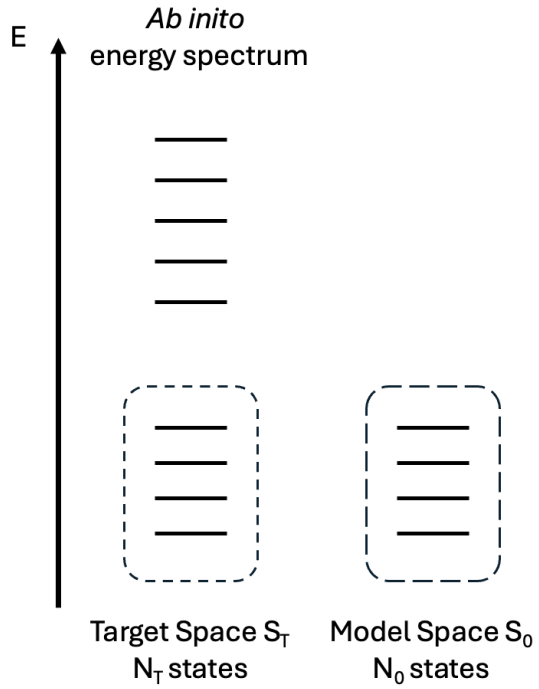

Figure 2.5: Schematic representation of the three spaces involved in effective Hamiltonian theory

Starting from the Schrodinger equation with the Born-Oppenheimer Hamiltonian $\hat{H}$:

$$\hat{H}\,|\Psi_m\rangle = E_m\,|\Psi_m\rangle \tag{2.2.20}$$

where Ψ_m are the eigenvectors with the associated eigenvalue E_m forming the space S of size N. We define a smaller space S_0 called model space with N_0 states $|\phi_i\rangle$, this space is usually composed of the low lying states where the model Hamiltonian will be developped. An effective Hamiltonian H_{eff} is built to reproduce the energy spectrum of the exact Hamiltonian in the target space S_T using a small number of low-lying states $\tilde{\Psi}_m$ such that:

$$\hat{H}_{eff}\,|\tilde{\Psi}_m\rangle = E_m\,|\tilde{\Psi}_m\rangle \tag{2.2.21}$$

This target space S_T is chosen to be of the same size as the model space S_0 allowing for direct comparison.

The first step is to project the eigenfunctions Ψ_m onto the model space using the projector:

$$\hat{P}_0 = \sum_m^{N_0} |\tilde{\phi}_m\rangle \langle\tilde{\phi}_m| \tag{2.2.22}$$

$$|\tilde{\Psi}_m\rangle = \hat{P}_0 |\Psi_m\rangle \tag{2.2.23}$$

These eigenvectors are not necesserilly orthogonal leading to a non-Hermitian Hamiltonian, this is problematic when comparing to the model Hamiltonians which are Hermitians. In this work, we apply the formalism proposed by Des Cloizeaux where the vectors are symmetrically orthogonalized from the overlap matrix S:

$$|\tilde{\Psi}^{\perp}_m\rangle = S^{-1/2} |\tilde{\Psi}_m\rangle \tag{2.2.24}$$

At this point, it is possible to check the quality of the model space by calculating the norm of the projected vectors present in the S matrix. If too small, the interactions of the system are not captured correctely by the model space making it inadequate.

When these projections are close to one, we can consider the model space adequate, the effective Hamiltonian is then built:

$$H_{eff} = \sum_m^N |\tilde{\Psi}^{\perp}_m\rangle E_m \langle\tilde{\Psi}^{\perp}_m| \tag{2.2.25}$$

Once this is done, this numerical matrix H_{eff} constructed from the *ab initio* exact Hamiltonian are compared to the model Hamiltonian representation matrix. This allows for the extraction of values for the model Hamiltonian parameters as well as a test of validity. If there is too much deviation between the two matrices, it is possible that there is some missing interaction in the model. In such a case, analytical derivation allows one to derive a new Hamiltoninan from a more sophisticated Hamiltonian.

Chapter 3

Study of the magnetic anisotropy in mononuclear complexes

The field of mononuclear complexes is a perfect area for the study of magnetic anisotropy. The finite size of such complexes as well as the localised character of the interaction allow for the explicit treatment of all atoms at play with reasonnable computational cost. This combined with the large amount of experimental data available allow for the validation of models and computational methodology. Numerous studies were dedicated to the application of the ZFS model Hamiltonian on mononuclear complexes based on fourth period transition metals. It has established that the value of the ZFS parameters are highly dependant on the metallic ion and its environment, the choice of ligand is crucial as we will see in this chapter.

State of the art methodology for such studies is to generate a wave-function from a CASSCF calculation including all electronic states generated by an active space composed of all the d orbitals of the metallic ion and the electrons occupying them. Dynamic correlation is taken into account by pertubation with NEVPT2. Spin orbit coupling between M_S components of all states are accounted for using Spin-Orbit-State-Interaction method with NEVPT2 correlated energies as the diagonal elements of the SO matrix. Finally, ZFS parameters are extracted using the Effective Hamiltonian Theory in a procedure implemented in the ORCA package.

3.1 First-Order Spin-Orbit Coupling

The ideal case for creating large anisotropy is to approach first order spin orbit coupling regime. First order spin orbit coupling arises when a two-fold or more degenerate ground state is formed from configurations with degenerate d-orbitals as represented on Figure 3.1 in case of d^6 configuration in D_{5h} geometry.

These two states would be strongly coupled via 1^{st}order SOC resulting in a large splitting of the M_S components of the ground state with a large value for the D term as strong as the spin orbit coupling constant. In reality a lift of degeneracy of the d orbitals is induced by a Jahn-Teller effect stabilising one of the two configurations, making it the main component of the ground state, and destabilising the other to an excited state. This loss of symmetry greatly reduces energy splitting of M_S component and may induce rhombicity in the system. At this stage the angular momentum L is quenched making the spin momentum S a "not-too-bad" quantum number, allowing the application of the ZFS model Hamiltonian formalism with the extraction of a D axial

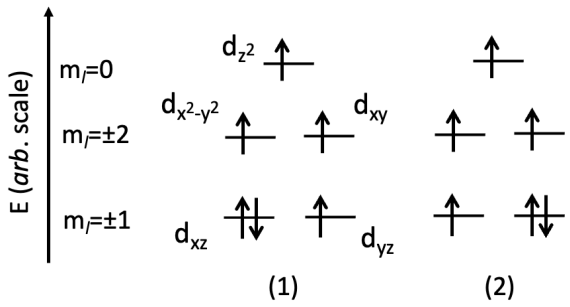

Figure 3.1: The two degenerate configurations for d^6 configuration in ideal D_{5h} geometry

parameter and rhombic terme E. The remaining anisotropy is the result of second order spin orbit coupling from the ground state with low-lying exicted states. This interaction stems from the excitation of an electron from a d orbital to a higher-energy orbital as depicted on Figure **??** and its magnitude rely on the difference in energy between the orbitals. Small energy differences (a few hundred cm^{-1}) between the orbital allow to retrieve a contribution of 1^{st}order SOC increasing the value of D. It has then become an interest to find ligands that satisfy this condition of quasi-degeneracy of the d-orbital.

With this in mind, a series of five Iron(II) complexes were synthesized in a heptacoordinated environment with different apical ligands (X and Y positions in Figure 3.2).

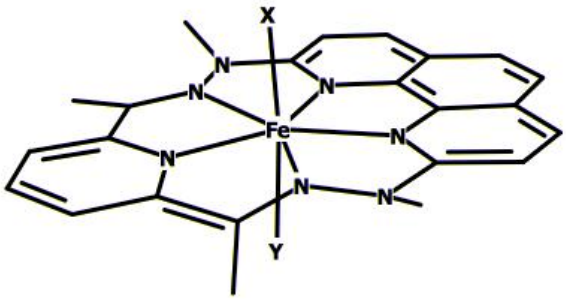

Figure 3.2: Schematic representation of the complex with H atoms attached to carbon hidden

3.2 Impact of the Electric field on the ZFS parameters

This chapter follows on from a previous study on a nickel II complex exhibiting strong uniaxial anisotropy. This complex has a tetradantate ligand (hexathyl-2,2',2"-triamino-triethylamine) in which three nitrogen atoms form bonds in the plane with the metal ion, while the fourth nitrogen atom forms a bond in the perpendicular plane, as shown in Figure 3.3. Opposite this fourth nitrogen atom is an apical halogenated ligand, either chlorine or bromine.

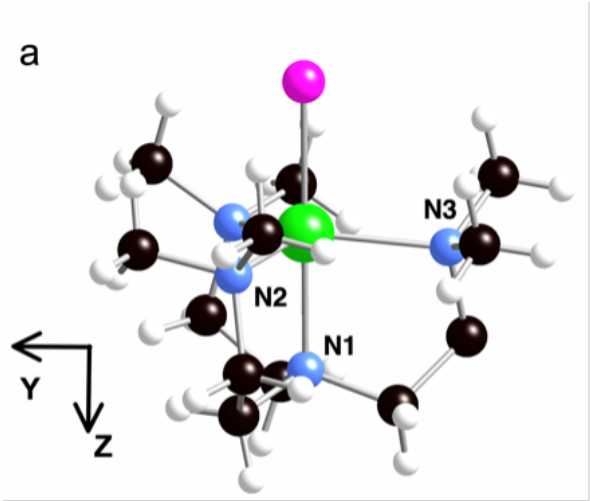

Figure 3.3: Representation of the complex [Ni(Me6trenCl)](ClO4), Ni in green, Cl, N in blue, C in black and H in white

Cristallographic data indicates that this complex crystallises in the trigonal space $R3c$ with a C_3 axis of symmetry along the Ni-Cl axis. This coordination induces a degeneracy of the d-orbital that share the same angular component m_l=$\pm$2($\pm$1), *i.e* $d_{xy}(dxz)$ and $d_{x^2-y^2}(d_{yz})$. The conditions for 1^{st} order SOC are met between two degenerate ground states carried by the two d^8 configurations depicted on Figure 3.4 This would result in a large splitting of the M_S components of the ground state with a large value for the D term as strong as the spin orbit coupling constant of the nickel ion (ξ_{Ni}=644cm^{-1}). At this point, a competing effect appears, the Jahn-Teller effect, which breaks the orbital degeneracy by distorting the ligand, reducing the axial anisotropy and gives rise to non-zero rhombic term (E$\neq$0). This distortion is confirmed by both electron paramagnetic resonance (EPR) studies and a theoretical study, which revokes of 1^{st}order SOC, leaving only 2^{nd}order SOC as the source of the anisotropy.

The ground state is now mainly carried by the configuration illustrated in Figure 3.4 where $d_{x^2-y^2}$ is simply occupied while d_{xy} remains doubly occupied. The concluding remark of this study was that this complex exhibits strong axial anisotropy with $D \approx -120cm^{-1}$ and a significant rhombic term E=1.6cm^{-1}. Although the Jahn-Teller effect has a significant impact on the value of the D parameter, it does not completely negate it, which shows that the ligand rigidity is on par with the distortion.

The focus of our study lies in the interest of controlling the anisotropy via an external stimulus, such as an electric field. While the effect of a magnetic field on the different M_S components is well understood in terms of the Zeeman effect, it is practically impossible to focus a magnetic field at the nanoscale. Electric fields, however, allow very accurate control at this scale and can affect the magnetic properties of a material

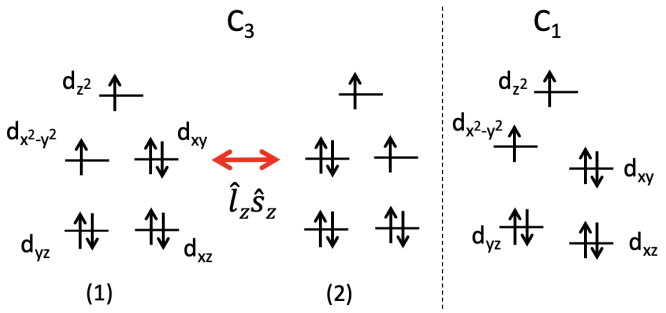

Figure 3.4: Energy diagrams of the d orbitals in case of three-fold symmetry C_3 (left) and in presence of Jahn-Teller distortion (right) with the induced lift of degeneracy of the d-orbitals.

via magneto-electric couplings. *Ab initio* calculations allow for the appreciation of the Jahn-Teller distortion as well as the determination of the anisotropic parameters D and E as functions of the applied electric field. Such a mechanism can be rationalized by analysing the spin-orbit coupled wave-function and the contribution of the excited states to the ZFS, both of which are provided by the ORCA program. It is believed that the origin of this magneto-electric effect comes from electronic and geometric structure changes under an applied electric field. To identify and quantify these mechanisms, the electric field was applied under two different orientations in three types of calculation, which allow us to quantify the following:

(a) eletronic structure changes, ZFS calculation under an applied field on the zero-field geometry

(b) geometric structure changes, ZFS calculation under no applied field on the field-optimised geometry.

(c) eletronic and geometric changes, both geometry optimisation and ZFS calculation performed under an applied electric field

In order to explore the response to the electric field for different orientations, the field F was initially applied along the Ni-Cl axis, which corresponds to the easy axis of magnetisation. This orientation includes the maximum component of the dipole moment and is referred to as F//Z. It was then applied perpendicular to this axis (F//Y) in the YZ plane containing the Ni, N1 and N3 atoms (see to Figure 3.3 for atom numbering). The YZ plane was chosen because the Ni-N3 bond length is the shortest of the three Ni-N bonds in the XY plane.

Analysis of the contribution

The main contribution to the D term comes from the SOC with the first excited triplet state (T^1), which is predominantly expressed in the determinant formedby exciting an electron from the $d_{x^2-y^2}$ to the d_{xy}. The Hamiltonian used to rationalise the SOC is given by $\hat{H}^{SO} = \sum_i \zeta(\hat{l}^i_x\hat{s}^i_x + \hat{l}^i_y\hat{s}^i_y + \hat{l}^i_z\hat{s}^i_z)$ where i runs over all the electrons in the d^8 configuration. The two lowest triplets are primarily formed from orbitals that are combinations of m_l=±2, the resulting SOC originates only from the part of the Hamiltonian involving the m_s=±1 of each triplet, *i.e* from the $\hat{l}^i_z\hat{s}^i_z$ term. This coupling stabilises the m_s=±1 of the T_0 ground state without affecting the m_s=0 component,

which gives a negative contribution to the D term. This contribution can be estimated using second-order perturbation theory:

$$C(D)^{(2)} = -\frac{|\langle T^0_{\pm 1}| \hat{H}^{SO} |T^1_{\pm 1}\rangle|^2}{\Delta E} \tag{3.2.1}$$

with $\Delta E = E(T^1) - E(T^0)$, the energy difference between the two states is given by ΔE. As this energy difference in energy is relatively small, a better treatment of the contributions can be obtained by diagonalising the 2×2 SOC matrices in the basis of $T^0_{\pm 1}$ and $T^1_{\pm 1}$ using a variational approach:

$$C(D)_{VAR} = \frac{\Delta E - \sqrt{\Delta E^2 + 4|SOC|^2}}{2} \tag{3.2.2}$$

where $|SOC|^2$ is the squared value of the off-diagonal term in the SO Hamiltonian between the ground and excited components. Other states may contribute positively or negatively to the overall value of D, their contributions can be obtained in the same way. The ORCA program also provides these contributions. To approach the actual value of D, one needs to sum all these contributions. However the variation of the electric field has almost no impact on the contributions of the excited states except for $T^1_{\pm 1}$, so they will be excluded from the rationalization. The rhombic term E will be rationalised, but as the sum of the contributions provided by the program does not match the overall variation of the E term, the analysis will be performed using wave functions.

3.2.1 Computational Informations

wave-function based calculations have been performed using the ORCA package. In a first place, Complete Active Space Self-Consistent Field calculations have been performed to account for non-dynamic correlations. The CAS(8,5) active space contains 8 electrons in the 5 essentially 3d orbitals of the Ni(II) ion, and two sets of orbitals have been optimized using an average procedure over all triplet and all singlet states of the configuration. To account for dynamic correlations at the 2nd order of perturbation, NEVPT2 calculations have been carried out for all states. The Spin-orbit State-Interaction method was then used to account for Spin-Orbit Couplings SOCs between the Ms components of all spin states using the NEVPT2 correlated energies as diagonal elements of the SO matrix. ZFS parameters were extracted using a procedure based on the effective Hamiltonian theory which proved to provide accurate values of the anisotropic parameters. The QZVPP extended basis sets have been used for Ni atoms (14s10p5d4f2g), SVP for H (2s1p) and TZVP for all other atoms (6s3p2d1f for N, 8s4p2d1f for Cl and 6s3p2d1f for C). As the field may change the geometrical structure, geometry optimizations were performed for different values and orientations of the field. We used the Hay-Wadt LanL2TZ(f) basis set for Ni and its corresponding relativistic effective core, Pople triple-ζ basis set (6-311G) for N and Cl atoms, a Pople double-ζ plus polarization basis set (6-31G*)26 for C atoms, and a Pople double-ζ basis set (6-31G) for H atoms and the B3LYP functional. Convergence thresholds for geometry optimization were set as VERYTIGHT.

The field will be applied in the two opposite directions referred as positive +F and negative –F with an amplitude of |F|= 1.028.109 V.m-1. The positive direction for the field in the Z direction induces an elongation of the Ni^{2+}-Cl^{-} bond, i.e., the positive

region of the electric potential is above Cl^- in Figure 1. The positive direction for the field in the Y direction induces an elongation of the Ni^{2+}-N_3, i.e., the positive region of the electric potential is to the right of N_3 in Figure 3.3.

3.2.2 Application of the electric field along the Z axis

First, we consider the field F along the Z axis, which carries the main component of the dipole moment. Table 3.1 shows the three components of the dipole moment and its magnitude. While not perfectly aligned, most of the component is along the Z axis, coinciding with the Ni-Cl bond while the X and Y components are small.

	μ_X	μ_Y	μ_Z	$\lvert\mu\rvert$
F=0	-0.0228007	-0.0772935	-8.1053645	8.1057651

Table 3.1: Dipole moment in Debye at F=0

Figure 3.5 shows the ground state energy as a function of the electric field for the three cases of calculation.

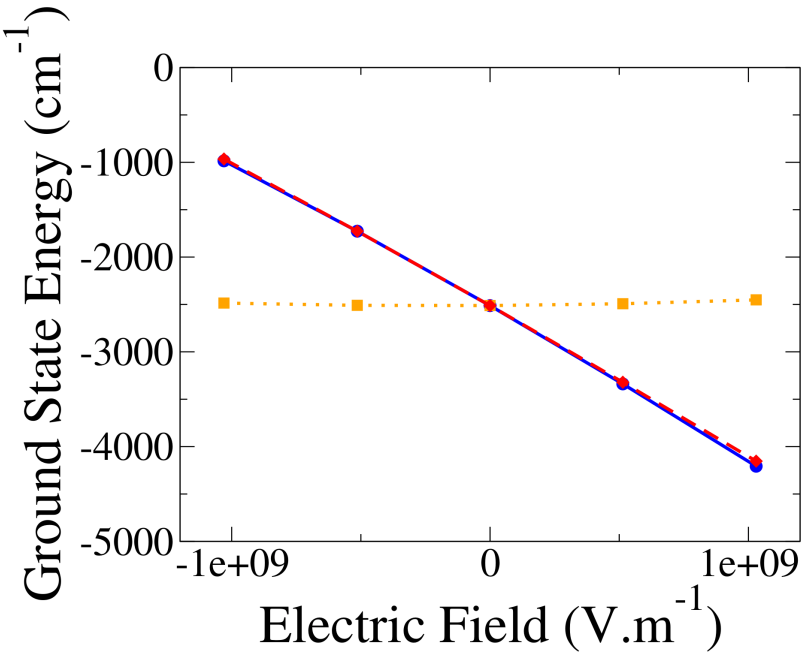

Figure 3.5: Energies in cm-1 (shifted by 58.35795.107 cm^{-1}) of the ground state obtained for the cases (a) (in blue and plain line), (b) (in orange and dotted line) and (c) (in red and dashed line) as functions of the field applied in the Z direction.

As expected from the Stark effect, the variation of case (a) is linear with respect to the fielf F, which tends to stabilise the ground state when he applied field and dipolar moment share the same orientation. In case (b) the energy follows a parabolic curve as the electric field disrupts the equilibrium geometry found at $F = 0V.m^{-1}$. The curvature is very small compared to the variation in case (a). The overall behaviour in case (c) follows the electronic effects in case (a).

Figure 3.6 shows how D parameter evolves as a function of the applied field F. In all three cases the absolute variation ($|dD/dF|$) is linear, with a negative slope in case (a)

and a positive slope in cases (b) and (c). This demonstrates that the geometric effects (b) have a stronger impact on the variation of the D value than electronic effects (a). Figure 3.7 shows the evolution of the E parameter. Although some deviation is observed for the geometric case (b), mainly due to the lack of precision in calculating this specific property, the overall variation is linear with the field. However, the variation in case (b) is very small ($<$0.05 cm^{-1}) and the behaviour of case (c) is now governed by the electronic effects with a negative absolute slope.

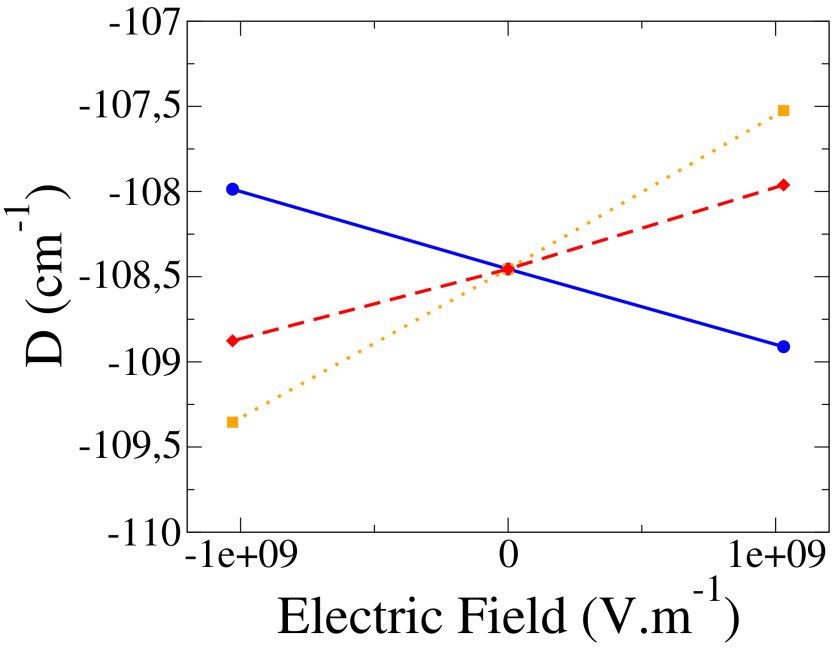

Figure 3.6: Evolution of the Axial D (left) parameter (in cm^{-1}) as a function of the field applied in cases (a) (in blue and plain line), (b) (in orange and dotted line) and (c) (in red and dashed line) in the Z direction

Table **??** shows the absolute slopes $|dD/dF|$ and $|dE/dF|$ for all three cases of calculations. Note that these slopes are additive with good precision.

$Hz/(V.m^{-1})$	(a) Electronic structure	(b) Geometric structure	(c) Both	Sum of (a) and (b)
$\|dD/dF\|$	-13.52	+26.66	+13.15	+13.14
$\|dE/dF\|$	-2.53	-0.36	-2.88	-2.89

Table 3.2: Slopes of the straight lines in cases (a), (b) and (c) for the D and E parameter for F//Z

To rationalise these results, the most significant contributions to the D parameter C(D) were examined as detailed in Table 3.3. As mentionned previously, the main contribution comes from the first excited triplet, and this contribution is also the most affected by the field F. While other states may have large contributions, the variation from $-F$ to $+F$ is minimal. Given that these contributions are positive it is clear that the first excited triplet is the main source of the substantial axial D parameter in this system.

The variation of the first excited triplet $\Delta C(D)_{VAR}$ matches well with that provided by ORCA, indicating that the variation of the SOC, as well as the variation of the

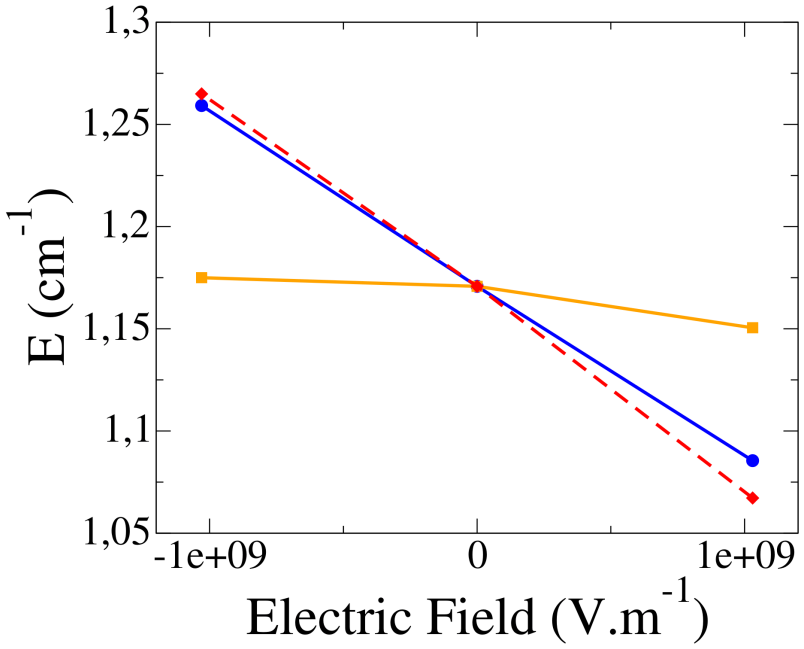

Figure 3.7: Evolution of the Rhombic E (right) parameter (in cm^{-1}) as a function of the field applied in cases (a) (in blue and plain line), (b) (in orange and dotted line) and (c) (in red and dashed line) in the Z direction

difference in energy $\Delta(\Delta E)$, can be used for the analysis. The perturbative estimation of this contribution yields a slightly larger value ($-193cm^{-1}$ at $F = 0$), as the two lowest states are rather close in energy ($\approx 2166cm^{-1}$), which takes them outside the pertubation regime. In case (a), the difference in energy between the two lowest triplet states remains roughly the same, so the variation of the SOC is the leading factor in the change of $|D|$. As the soc increases, so does D. The opposite is seen in case (b) where the leading factor is the change in energy of the two states. The energy difference increases, so $|D|$ decreases as can be deduced from the perturbative expression of the contribution 3.2.1. The overall changes in $|D|$, case (c), follows the same behaviour as in case (b), as the energy difference remains the dominant factor indicating that the geometrical structure dominates. This can be explained by the changes in geometry under the application of the eletric field, as reported in Table 3.4, with the variation of the distances between the Ni(II) ion and its coordination sphere between $+F$ and $-F$. The Ni-Cl bond length increases in a positive field $+F$, as this bond carries most of the dipole moment and is therefore expected to lengthen in order to maximise its interactions with the field. However, the others atoms tend to move closer to the Ni(II) ion, increasing the ligand field in the XOY plane.

This destabilises both the $d_{x^2-y^2}$ and d_{xy} orbitals, the former, which points directly towards N_3 is more affected. This leads to an increase in the energy difference between these orbitals and thus between the ground and excited states. As can be seen from Tables 3.3 and 3.5, the variation of the two differences in energy follows the same pattern in each case of calculation.

The rhombic term E describes the difference in anisotropy between the X and Y axes. For its rationalisation, the same analysis as that applied tothe D term should be

	Excited state	C(D) for -F	C(D) for +F	$\Delta C(D)$ ORCA	$\Delta C(D)$ VAR.	$\Delta C(D)$ PERT.	$\Delta\|SOC\|^2$	$\Delta(\Delta E)$
(a)	T_1	-179.18	-180.06	-0.88	-0.82	-0.96	1722.78	-1.60
	T_2	23.84	23.72	-0.12				
	T_3	19.61	19.68	0.07				
	S_3	20.48	20.57	0.09				
(b)	T_1	-180.95	-178.25	2.70	2.70	3.42	-209.90	36.2
	T_2	23.82	23.72	-0.10				
	T_3	19.71	19.58	-0.13				
	S_3	20.55	20.51	-0.04				
(c)	T_1	-180.49	-178.66	1.83	1.90	2.47	1509.15	34.7
	T_2	23.88	23.66	-0.22				
	T_3	19.67	19.61	-0.06				
	S_3	20.51	20.56	0.05				

Table 3.3: Contributions to the axial parameter D (in cm-1) of the most contributing excited states and their variations ΔC(D) between the -F and +F in the Z direction either provided by ORCA, calculated variationally and perturbatively. Δ|SOC|2 is the variation of the square of the module of the SOC between the ground and the first excited triplet states while Δ(ΔE) is the variation between the -F and +F of their energy difference (in cm^{-1}) obtained at the NEVPT2 level.

Ligands	$-F$	$+F$	$\Delta(distance)$
Cl	2.31391	2.32709	$131.8.10^{-4}$
N_1 (apical)	2.2.15016	2.14727	$-28.9.10^{-4}$
N_2	2.22739	2.22043	$-69.6.10^{-4}$
N_3	2.14628	2.14139	$-48.9.10^{-4}$
N_4	2.22688	2.22023	$-6.65.10^{-4}$

Table 3.4: Variation of the distances in Angstrom between the Ni(II) ion and the closest atoms of the ligand between $-F$ and $+F$ with F//Z.

used, based on the contributions provided by ORCA. Unfortunately these contributions cannot be used because their sum increases with the field while the E values extracted via effective Hamiltonian theory decrease as shown in Figure 3.7. Nevertheless it is possible to rationalise the E term by identifying the determinants that distinguish the X direction from the Y direction. In the case of an applied field along the Z axis, the $d_{x^2-y^2}$,d_{xy} and d_{z^2} orbitals are symmetric in X and Y. As such the only determinants that treat these two directions differently are those with a single occupation in the d_{xz} or d_{yz}. There are six of these determinants with M_S=1, two of them have the largest coefficients in the wave-function of the T_2 and T_3 excited states, resulting from single excitation from either of these orbitals to the $d_{x^2-y^2}$ or d_{z^2} which are singly occupied in the ground state T_0. If there is no difference between the two directions, *i.e* no rhombicity E=0, the weights of these determinants should be the same in both states leading to two contributions that cancel each other out. To estimate the evolution of the rhombicity, one can look at the variation of these weights with respect to the field. We can define $\Delta w(X-Y)$ which is the difference between the weight w(d_{xz}) and w(d_{yz}), and its overall variation $\Delta(\Delta w(X-Y))$ as reported in Table 3.6.

Firstly, we can observe the small variation in case (b) which matches well the variation of E for this case in 3.7. The variation $\Delta(\Delta w(X-Y))$ is very similar between case (a) and case (c), which confirms that the overall variation of the E term is dictated by the changes in the electronic structure induced by the application of the electric field.

Variation of the orbital energy differences	(a)	(b)	(c)
$\Delta(\Delta\epsilon(d_{x^2-y^2} - d_{xy}))$	6.58	258.98	267.76

Table 3.5: Variation between $-F$ and $+F$ applied in the Z direction of the orbital energy difference $\Delta(\Delta\epsilon(d_{x^2-y^2} - d_{xy}))$ in cm^{-1}

		$-F$	$-F$	$\Delta(\Delta w(X-Y))$
(a)	$w(d_{xz})$	96.200	96.741	-0.528
	$w(d_{yz})$	97.210	97.224	
	$\Delta w(X-Y)$	1.010	0.482	
(b)	$w(d_{xz})$	96.543	96.494	0.088
	$w(d_{yz})$	97.282	97.145	
	$\Delta w(X-Y)$	0.739	0.651	
(c)	$w(d_{xz})$	96.271	96.762	-0.621
	$w(d_{yz})$	97.282	97.152	
	$\Delta w(X-Y)$	1.011	0.390	

Table 3.6: Weight w(d_{xz}) and w(d_{yz}) of the determinants with single occupation in the respective orbitals, their difference $\Delta w(X-Y)$ and their overall variation $\Delta(\Delta w(X-Y))$ in all three case of calculation for F//Z.

3.2.3 Application of the electric field along the Y axis

Now, let's consider the applied field in the Y direction $F//$Y. The field is now perpendicular to the main component of the dipole moment (μ_Z). Note that the field is not applied directly along the Ni-N_3 bond, which is slightly out of the XoY plane, but rather along the Y axis which is perpendicular to the Z axis. Figure 3.8 shows the evolution of the ground state energy when $F//$Y. Case (b) follows the same parabolic trend as when $F//$Z, the argument remains the same. The situation differs from that of F//Z in case (a), the evolution is now quadradic rather than linear. The applied field induces a change in the sign of the dipole moment component μ_y which is very small, see Table 3.1. The Stark effect then stabilises the ground state for both signs of the electric field F.

Figure 3.9 shows the evolution of the D term with respect to the applied field. It once again follows a linear behavior in all three cases. The sign of the slopes has now inverted, with $|dD/dF|$ being positive for case (a) and negative for cases (b) and (c) as opposed to when the field was along the Z direction.

The slopes for each case are shown in Table 3.7, once again the variation of the D term is dictated by the geometrical changes under the applied field, case (b). Note that the slopes $|dD/dF|$ are very much additive and now much higher in the F//Y case than in the F//Z case, almost seven times larger.

$Hz/(V.m^{-1})$	(a) Electronic structure	(b) Geometric structure	(c) Both	Sum of (a) and (b)
$\|dD/dF\|$	+25.32	-110.75	-85.45	-85.43
$\|dE/dF\|$	-2.39	+1.20	-1.19	-1.19

Table 3.7: Slopes of the straight lines in cases (a), (b) and (c) for the D and E parameter for F//Y

The most significant contributions are reported in Table 3.8. Once again, the contribution that is the most affected by the electric field is that of the first excited state T^1 with good agreement between the ORCA and the variational/perturbative estimations.

In case (a), note the increase in the energy difference $\Delta(\Delta E)$. This is due to a

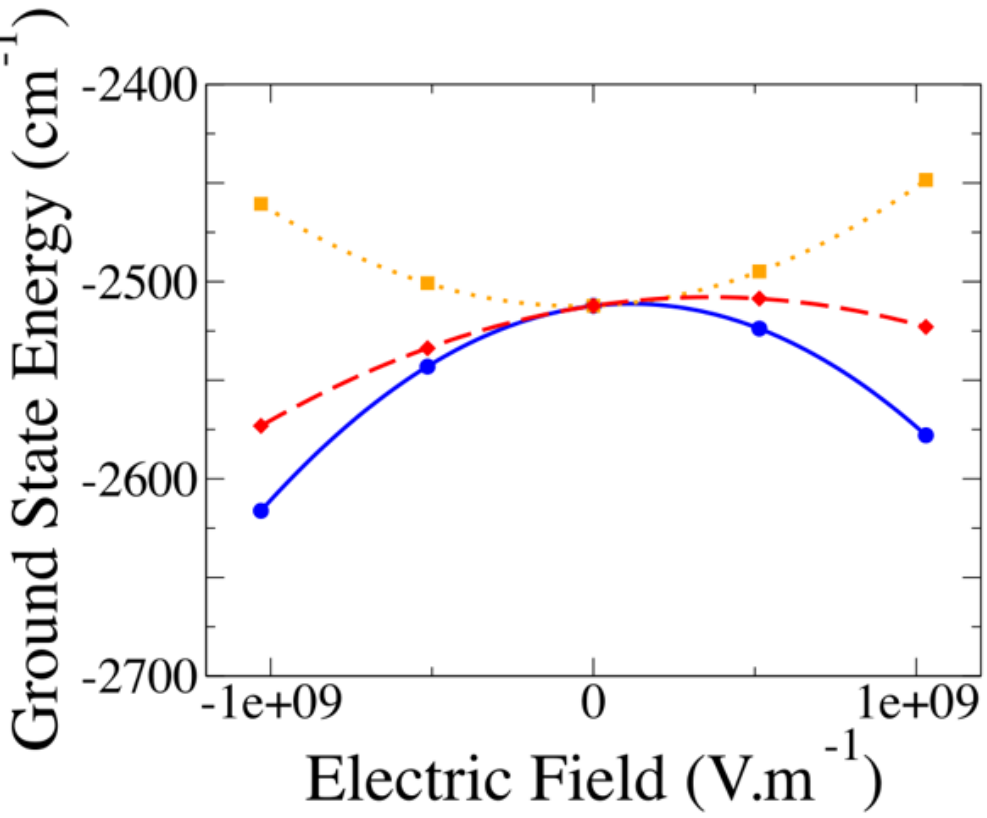

Figure 3.8: Energies in cm-1 (shifted by 58.35795.107 cm^{-1}) of the ground state obtained for the cases (a) (in blue and plain line), (b) (in orange and dotted line) and (c) (in red and dashed line) as functions of the field applied in the Y direction.

deformation of the electronic could around the Ni(II) ion in the direction of N_3 for $+F$. This destabilises the $d_{x^2-y^2}$ orbital, which points directly towards N_3 and stabilizes the d_{xy} orbital, resulting in an increase in the energy difference between the two states.

The rationalization of the variations for case (b) can be explained by the evolution of the ligand field shown in Table 3.9. The application of the electric field alond the Y direction tends to elongate the Ni-N_3 bond and concomitantly reduces the other Ni-N bond lengths in the XY plane. The ligand field along the Y axis is therefore reduced stabilising the $d_{x^2-y^2}$ orbital while the d_{xy} orbital, which points directly towards N_2 and N_4, is destabilised. This results in a decrease in the orbital energy difference $\Delta(\Delta\epsilon(d_{x^2-y^2} - d_{xy}))$, thus decreasing the energy difference between the ground state T^0 and the excited state T^1. According to eq 3.2.1, this leads to an increase in the magnitude $|D|$,as can be seen in Figure 3.9 for case (b). Note that the impact of the electric field on the geometric structure results in the greatest change of magnitude $|D|$ with a slope as large as $-110.75Hz/(V.m^{-1})$. This is due to the large variation in the energy difference $\Delta(\Delta E)$ for case (b) which is one order of magnitude greater than when the field is along the Z axis. Similarly to the F//Z case, the overall trend in the evolution of the axial anisotropy D is driven by the field's impact on the geometric structure.

As for rhombicity, changes in the electronic structure caused by the application of an

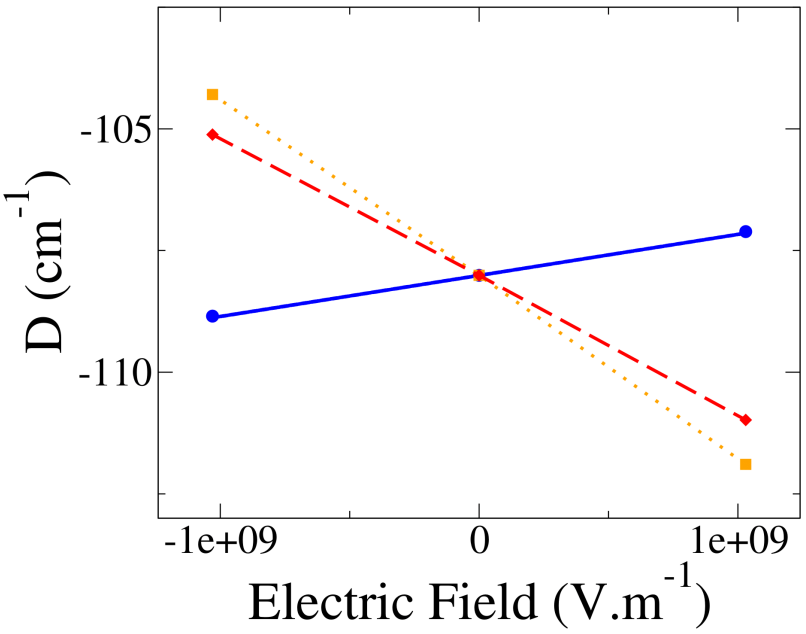

Figure 3.9: Evolution of the Axial D (left) parameter (in cm^{-1}) as a function of the field F//Y in cases (a) (in blue and plain line), (b) (in orange and dotted line) and (c) (in red and dashed line)

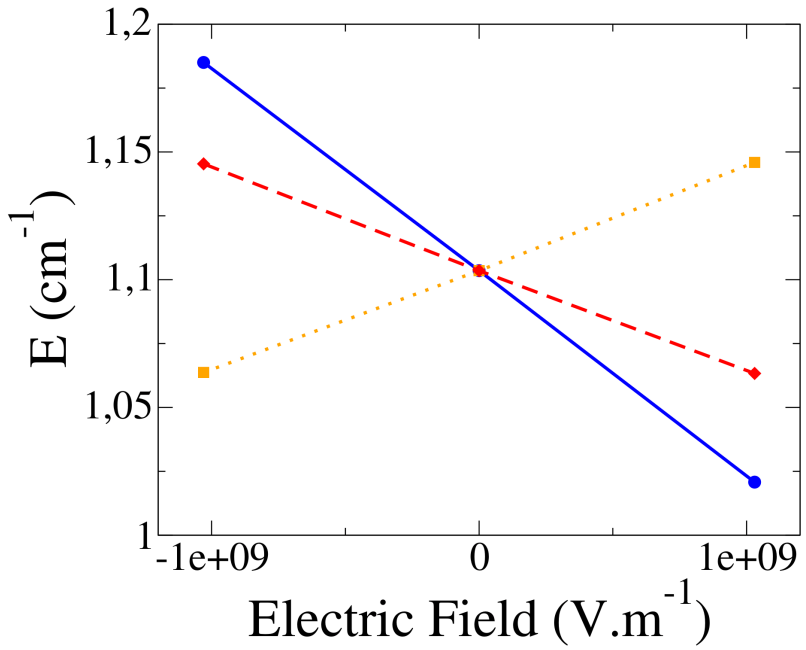

Figure 3.10: Evolution of the Rhombic E (right) parameter (in cm^{-1}) as a function of the field F//Y in cases (a) (in blue and plain line), (b) (in orange and dotted line) and (c) (in red and dashed line)

electric field are once again responsible for the overall variation as indicated by Table 3.7. These variations are linear with good additivity but are smaller than observed when

	Excited state	C(D) for -F	C(D) for +F	$\Delta C(D)$ ORCA	$\Delta C(D)$ VAR.	$\Delta C(D)$ PERT.	$\Delta\|SOC\|^2$	$\Delta(\Delta E)$
(a)	T_1	-179.99	-178.26	1.73	1.74	2.21	36.05	24.40
	T_2	23.66	24.05	0.39				
	T_3	19.60	19.61	0.01				
	S_3	20.53	20.50	-0.03				
(b)	T_1	-174.84	-183.67	-8.83	-8.76	-11.10	-162.22	-122.40
	T_2	23.91	23.82	-0.09				
	T_3	19.56	19.65	0.09				
	S_3	20.44	20.60	0.16				
(c)	T_1	-175.65	-182.86	-7.11	-7.02	-8.91	-124.89	-98.20
	T_2	23.71	24.02	0.31				
	T_3	19.56	19.65	0.09				
	S_3	20.45	20.59	0.14				

Table 3.8: Contributions to the axial parameter D (in cm-1) of the most contributing excited states and their variations ΔC(D) between the -F and +F in the Y direction either provided by ORCA, calculated variationally and perturbatively. Δ|SOC|2 is the variation of the square of the module of the SOC between the ground and the first excited triplet states while Δ(ΔE) is the variation between the -F and +F of their energy difference (in cm^{-1}) obtained at the NEVPT2 level.

Ligands	$-F$	$+F$	$\Delta(distance)$
Cl	2.32024	2.32043	$2.4.10^{-4}$
N_1 (apical)	2.14947	2.14727	$1.7.10^{-4}$
N_2	2.22518	2.22245	$-27.3.10^{-4}$
N_3	2.1482	2.14596	$11.4.10^{-4}$
N_4	2.2270	2.22229	$-4.1.10^{-4}$

Table 3.9: Variation of the distances in Angstrom between the Ni(II) ion and the closest atoms of the ligand between $-F$ and $+F$ with F//Y.

F//Z. Figure 3.10 shows that the rhombic E decreases as the field increases, indicating that the difference between the X and Y axes diminishes. This can be explained by the evolution of the weights $w(d_{xz})$ and $w(d_{yz})$ of determinants with a single occupation in the d_{xz} and d_{yz} orbitals, which are found in Table 3.10. In case (a) and (c), the diffence $\Delta(X-Y)$ of the weights between X and Y decreases with the field, which reduces the rhombicity term E. Note that $\Delta(X-Y)$ is positive in case (b) which is consistent with the positive slope observed for geometric structure changes in Table 3.7 and Figure 3.10.

		$-F$	$-F$	$\Delta(\Delta w(X-Y))$
(a)	$w(d_{xz})$	96.603	96.738	-0.174
	$w(d_{yz})$	97.191	97.152	
	$\Delta w(X-Y)$	0.588	0.414	
(b)	$w(d_{xz})$	96.661	96.695	+0.002
	$w(d_{yz})$	97.159	97.195	
	$\Delta w(X-Y)$	0.498	0.500	
(c)	$w(d_{xz})$	96.597	96.762	-0.170
	$w(d_{yz})$	97.175	97.170	
	$\Delta w(X-Y)$	0.578	0.480	

Table 3.10: Weight w(d_{xz}) and w(d_{yz}) of the determinants with single occupation in the respective orbitals, their difference $\Delta w(X-Y)$ and their overall variation $\Delta(\Delta w(X-Y))$ in all three case of calculation for F//Y.

3.2.4 Conlcusion

The aim of this study was to determine the influence of an external electric field on the anisotropy parameter of the ZFS Hamiltonian in a Ni(II) complex close to first-order spin-orbit coupling regime. A combination of DFT and wave-function theory was employed to evaluate the geometric changes induced by the field and extract the parameter using effective Hamiltonian theory. Treating the electronic and geometric changes separately allowed us to identify the mechanisms responsible for the variation in the parameters. Two orientations for the field were explored. Depending on which parameter it affected the most, both orientations proved to be of interest. The findings can be summarised in a few points:

(i) The rhombicity of the system, described by the rhomic term E, can be modulated by the electric field. The variation dE/dF can be significant, especially for F//Z which was not expected at first. As rhombicity describes the anisotropy between the X and Y axes, it seems reasonnable to assume that it would be more affected by the field oriented in the XY plane than in the Z direction. However, the most important contributions to the E term were found to come from excited states (T^2 and T^3) coupled to the ground state via excitations from the d_{xz} or the d_{yz} orbitals to the d_{z^2} or the $d_{x^2-y^2}$ orbitals. As these orbitals are mainly oriented along the Z axis, it is therefore natural that these excitations would be more impacted by the field along the Z directions than in the XY plane.

(ii) The electronic and geometric changes have an opposite effect on the variation dD/dF for both field orientation. In case (a) for F//Z, the large increase in magnitude $|D|$ can be related to a large variation of the SOC while the energy difference ΔE between T^0 and T^1 drecreases. When F//Y, the variations are governed only the difference in energy ΔE between the two lowest triplet. In case(a), the electronic cloud displacement induced by the electric field tend to stabilise the d_{xy} orbital and destabilise the $d_{x^2-y^2}$ orbital leading to an increase of ΔE

(iii)

Chapter 4

Electric field on Exchange anisotropy

Numerous studies have been conducted to characterise the properties of magnetic anisotropies and many successful procedures have been developed with great success as discussed above. However, only a few studies have been applied to determine the properties of the exchange anisotropy using Quantum Chemistry theories. This study is part of a series of works that aims to rationalise the origin of exchange anisotropy in polynuclear molecules. The spin Hamiltonian used to describe anisotropic behaviour in binuclear systems is as follows:

$$\hat{H}_{AB} = J_{AB}\hat{\mathbf{S}}_A \cdot \hat{\mathbf{S}}_B + \hat{\mathbf{S}}_A \cdot \overline{\overline{D}}_{AB} \cdot \hat{\mathbf{S}}_B + \mathbf{d}_{AB} \cdot (\hat{\mathbf{S}}_A \times \hat{\mathbf{S}}_B) \tag{4.0.1}$$

To achieve this, a procedure for extracting values of the Dzyaloshinskii-Moriya pseudovector interaction and the symmetric exchange anisotropy D_{ij}-tensor using effective Hamiltonian theory in combination with wave-funcion based method.

This procedure was tested on a simple model molecule, shown in Figure 4.1, consisting of two Cu^{2+} cations separated by Cl^{-} anions.

The reason for choosing this system is its simplicity, with only one magnetic electron per centre and a reasonable size, it allows for simple analytical derivation and high-level treatment of the correlation. Such a toy molecule can also be modelled to assess the impact of geometry, *i.e* distances and angles, on these interactions. Initially, it was determined that the most favourable setting for obtaining large values of the anisotropic interactions is to approach first-order coupling regime without reaching it. This situation arises when the outside angle ϕ reaches 120°, at which point the local environment of each Cu^{2+} is close to a C_3-axis symmetry. This allows the condition of quasi-degeneracy of the $d_{x^2-y^2}$ and d_{xy} orbitals to be achieved. However, due to the D_{2h} symmetry of the system, it possesses an inversion centre, leading to a zero value of DMI. To induce a non-zero value of the DMI, the first two studies relied on the deformation of the molecule with a variation of the θ angle, which resulted in the hybridization of the otherwise pure cartesian d-orbitals. This mixing of the d-orbitals is key to creating DMI, as increasing the mixing was shown to allow very large values of DMI to be obtained. It was then thought that applying of an external electric field could have the same effect on a smaller scale by acting on the electronic could itself rather than the nuclei's position. As mentionned in the previous chapter, an electric field is an interesting option as it can be focused accurately at the molecular level. Using an external stimulus is also much easier than relying on the "intrinsic" geometry of the molecule. In a following work, the impact of the electric field on the isotropic and antisymmetric exchange spin Hamiltonian parameter was determined, establishing that

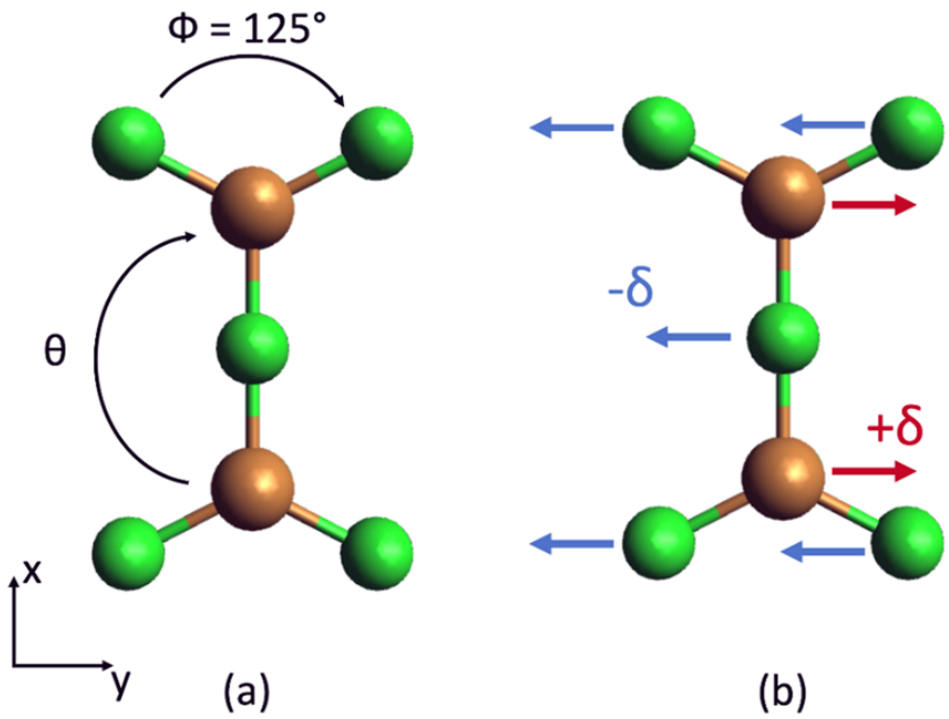

Figure 4.1: (a) Cu_2Cl_5 model molecule of D_{2h} symmetry, (b) displacement δ of the atoms generated by the application of an electric field along the y direction.

the Dzyaloshinskii-Moriya pseudo-vector is highly sensitive to the external field. Here we follow the already established procedure to focus our attention on the symmetric exchange anisotropy tensor. The work proceeds along two axes:

(i) Derive an appropriate model to estimate the symmetric tensor under the condition of 1^{st} order SOC in the absence of an electric field.

(ii) Study how the symmetric tensor varies under the influence of an electric field, and how this affects the DMI.

4.1 Computational Informations

The eletronic and relativistic state computation were performed using the MOLCAS code. Complete-Active-Space-Self-Consistent field calculations were carried out for various values of the angle Φ, ranging from $\Phi = 130°$ (close to 1^{st} order SOC) to 170° (far from it). The active space consists of six electrons occupying the $d_{x^2-y^2}$ and d_{xy} orbitals of each copper centre, CAS(6,4), with two sets of orbitals optimised in an average way. One for the four lowest triplet states and the other for the four lowest singlet states. An enlarged active space containing all d-orbitals and their electrons, CAS(18,10) was also considered, but a previous study showed that it had little impact on the extracted parameters and that the reduced active space CAS(6,4) was sufficient to capture the effect of first-order SOC. Nevertheless, it used for the treatment of second-order spin orbit coupling.

Dynamical correlation was introduced using the Difference-dedicated-configuration-interaction (DDCI3) method, perfored using the CASDI code interfaced with the MOLCAS chain. Three types of SO-SI calculation were performed:

(i) CAS(6,4)SCF : the energy and wave-function are obtained from CASSCF calculation

(ii) CAS(6,4)DDCI/SCF-SO : the DDCI energy are used while the wave-function remain that of the CAS(6,4)SCF

(iii) CAS(6,4)DDCI/DDCI-SO : the energy and wave-function are obtained from DDCI calculation

This allows to study the impact of each component of dynamic correlation (energy or wave-function) on the exchange interactions. The TZVP basis set were used throughout all calculations: 5s4p3d1p for Cu and 4s3p1d for Cl.

The continious electric field was added in the SEWARD stage of the calculation in MOLCAS, the X,Y and Z directions were treated but most of the results reported here relates to the Y direction.

4.2 Theorical model

In order to derive the parameters of the Multispin Hamiltonian, we must first define the model space. Let a (a') and b(b') represent the magnetic orbitals located on each copper ion. These orbitals are obtained from state-specific calculations and may differ between triplet and singlet states by the tails on the Cl^- ligands hence the difference of notation. With the application of an electric field, one can predict that the otherwise pure cartesian orbitals $d_{x^2-y^2}$ and d_{xy} will hybridise to form the orbitals $a(a')$ and $b(b')$. We refer to the orthogonal cartesians orbitals as $a_1(b_1)$ and $a_2(b_2)$ respectively depending wether the site is A or B.

$$a = \alpha a_1 + \beta a_2 \qquad b = -\alpha b_1 + \beta b_2 \qquad a' = \alpha' a_1 + \beta' a_2 \qquad b' = -\alpha' b_1 + \beta b_2 \quad (4.2.1)$$

Where $\alpha(\alpha')$ and $\beta(\beta')$ are the mixing coefficients between the d orbital in the triplet(singlet) state. The coupling between the lone electron of each copper ion gives rise to a triplet and singlet state that will form the basis of the model space:

$$T^+ = |ab| \quad (4.2.2)$$

$$T^0 = \frac{1}{\sqrt{2}}(|a\overline{b'}| - |b\overline{a'}|) \quad (4.2.3)$$

$$T^- = |\overline{a}\overline{b}| \quad (4.2.4)$$

$$S = \frac{1}{\sqrt{2}}(|a'\overline{b'}| + |b'\overline{a'}|) \quad (4.2.5)$$

The matrix representation of the Multi-Spin Hamiltonian in this basis is:

H_{MS}	T^+	T^0	T^-	S
T^+	$\frac{J_{AB}}{4} + \frac{D_{zz}}{4}$	$\frac{D_{xz}-iD_{yz}}{2\sqrt{2}}$	$\frac{(D_{xx}-D_{zz}-2iD_{xy})}{4}$	$\frac{d_y+id_x}{2\sqrt{2}}$
T^0	$\frac{D_{xz}+iD_{yz}}{2\sqrt{2}}$	$\frac{J_{AB}}{4} - \frac{D_{zz}}{4} + \frac{(D_{xx}+D_{yy})}{4}$	$-\frac{D_{xz}-iD_{yz}}{2\sqrt{2}}$	$-\frac{id_z}{2}$
T^-	$\frac{(D_{xx}-D_{zz}+2iD_{xy})}{4}$	$-\frac{D_{xz}+iD_{yz}}{2\sqrt{2}}$	$\frac{J_{AB}}{4} + \frac{D_{zz}}{4}$	$\frac{d_y-id_x}{2\sqrt{2}}$
S	$\frac{d_y-id_x}{2\sqrt{2}}$	$\frac{id_z}{2}$	$\frac{d_y+id_x}{2\sqrt{2}}$	$-\frac{3J_{AB}}{4} - \frac{D_{zz}}{4} - \frac{(D_{xx}+D_{yy})}{4}$

The evolution of the J_{AB} and the components d_x, d_y and d_z under the application of an external electric field has been studied previously. The components D_{xx}, D_{xy}, etc. are

the components of the symmetric exchange anisotropy $\overline{\overline{D}}$-tensor which is the focus of this study. Its evolution will be compared to previous results, especially those relating to the DMI.

When approaching the condition of quasi-degeneracy of the $d_{x^2-y^2}$ and d_{xy} orbitals, *i.e* first-order spin orbit coupling, second-order perturbation theory cannot be used to account for spin-orbit coupling due to the small differences in energy between the lowest states. Therefore, a variational treatment is mandatory. To this end, a model was derived to assess the contribution of 1^{st} order SOC based on the spin-free states generated by the occupation of these two orbitals. The following states form the uncoupled basis:

$$\begin{aligned}
T_1^+ &= |a_1 b_1|; \qquad T_1^0 = \frac{|a_1\overline{b}_1| - |b_1\overline{a}_1|}{\sqrt{2}} \\
S_1 &= \frac{|a_1\overline{b}_1| - |b_1\overline{a}_1}{\sqrt{2}} \\
T_2^+ &= \frac{|a_1 b_2| + |b_1 a_2|}{\sqrt{2}}; \qquad T_2^0 = \frac{|a_1\overline{b}_2| + |b_1\overline{a}_2| - |a_2\overline{b}_1| - b_2\overline{a}_1|}{2} \\
S_2 &= \frac{|a_1\overline{b}_2| + |b_1\overline{a}_2| + |a_2\overline{b}_1| + b_2\overline{a}_1|}{2} \\
T_3^+ &= \frac{-|a_1 b_2| + |b_1 a_2|}{\sqrt{2}}; \qquad T_3^0 = \frac{-|a_1\overline{b}_2| + |b_1\overline{a}_2| - |a_2\overline{b}_1| + b_2\overline{a}_1|}{2} \\
S_3 &= \frac{-|a_1\overline{b}_2| + |b_1\overline{a}_2| + |a_2\overline{b}_1| - b_2\overline{a}_1|}{2} \\
T_4^+ &= |a_2 b_2|; \qquad T_4^0 = \frac{|a_2\overline{b}_2| - |b_2\overline{a}_2|}{\sqrt{2}} \\
S_4 &= \frac{|a_2\overline{b}_2| - |b_2\overline{a}_2|}{\sqrt{2}}
\end{aligned} \tag{4.2.6}$$

For simplicity, the ionic part of these states was left out of the model, but will be taken into account in the *ab inito* calculations as they play an essential part in the antiferromagnetic coupling. Note that, in absence of electric field, crystal field theory indicates that the magnetic orbitals are the $d_{x^2-y^2}$ on each copper center. Thus the energy ordering should follow the order in which they are expressed in 4.2.6. The spin-orbit matrix can be derived from the SO-Hamiltonian:

$$\hat{H}^{SO} = \zeta(\hat{l}_1\hat{s}_1 + \hat{l}_2 + \hat{s}_2) \tag{4.2.7}$$

With $\hat{l}_i$ the angular momenta and $\hat{s}_i$ the spin momenta operators working on electron i and ζ the spin-orbit constant. The spin-orbit couplings between the states 4.2.6 originate from the $\hat{l}_z\hat{s}_z$ part of the $\hat{H}^{SO}$ that couples the determinants formed from orbitals of same spatial (m_l) and spin (m_s) component. The representation matrix of this Hamiltonian is given in the basis developped in eq 4.2.6 with the addition of electronic couplings.

The electronic effects included are the isotropic couplings J_i, between triplet and singlet states of the same spatial nature. The $h_i(h_i$') couplings are induced by the mixing of the the $d_{x^2-y^2}$ and d_{xy} orbitals when the electric field is applied along the Y

$\hat{H}^{SO}$	$\|T_1^+\rangle$	$\|T_2^+\rangle$	$\|T_3^+\rangle$	$\|T_4^+\rangle$	$\|T_1^0\rangle$	$\|T_2^0\rangle$	$\|T_4^0\rangle$	$\|S_1\rangle$	$\|S_3\rangle$	$\|S_4\rangle$
$\langle T_1^+\|$	E_1+J_1	h_1	$i\zeta\sqrt{2}$	δ_4	0	0	0	0	0	0
$\langle T_2^+\|$	h_1	E_2+J_2	0	h_2	0	0	0	0	0	0
$\langle T_3^+\|$	$-i\zeta\sqrt{2}$	0	E_3+J_3	$i\zeta\sqrt{2}$	0	0	0	0	0	0
$\langle T_4^+\|$	δ_4	h_2	$-i\zeta\sqrt{2}$	E_4+J_4	0	0	0	0	0	0
$\langle T_1^0\|$	0	0	0	0	E_1+J_1	h_1	δ_4	0	$-i\zeta\sqrt{2}$	0
$\langle T_2^0\|$	0	0	0	0	h_1	E_2+J_2	h_2	$-i\zeta\sqrt{2}$	0	$-i\zeta\sqrt{2}$
$\langle T_4^0\|$	0	0	0	0	δ_4	h_2	E_4+J_4	0	$-i\zeta\sqrt{2}$	0
$\langle S_1\|$	0	0	0	0	0	$i\zeta\sqrt{2}$	0	E_1	h_1'	δ_4'
$\langle S_3\|$	0	0	0	0	$i\zeta\sqrt{2}$	0	$i\zeta\sqrt{2}$	h_1'	E_3	h_2'
$\langle S_4\|$	0	0	0	0	0	$i\zeta\sqrt{2}$	0	δ_4'	h_2'	E_4

Table 4.1: Representation matrix of $\hat{H}^{SO}$ and electronic couplings in the uncoupled basis. T_3^0 and S_2 are not coupled to the others, as such they were left out for clarity. $h_1(h_1$') and $h_2(h_2')$ are couplings induced by the electric field and differ between triplet and singlet states by their exchange integrals. δ_1 and δ_2 are small bielectronic integrals between $T_1(S_1)$ and $T_4(S_4)$. The M_S=-1 components of the triplets are left out but possess the same couplings as the M_S=1 components.

direction. This coupling gives rise to the DMI in this system, as it opens coupling path between S_1 and T_1^0. The couplings can be estimated perturbatively at second-order, but as the system enters 1^{st} order SOC the best approach is to diagonalise the matrix. In order to understand the origins of the anisotropic parameter, D_{AB} and the DMI, the couplings must be decomposed according to their contributions. Put simply, the D_{AB} describes the difference in energy between the M_S=$\pm$ 1 and the M_S=0 components. Within this model space, there is no difference in the couplings between the two M_S=$\pm$1 components of this matrix. As such there is no rhombic term E_{AB}, when considering only first-order SOC. Hence to estimate the D_{AB}, one has to look for states coupled to either T_1^0 or T_1^+. The T_1^+ component is coupled via SOC to T_3^+ which stabilises it, bringing a negative contribution to the D_{AB} by reducing the energy of the M_S=$\pm$1 component. On the other hand, the S_3 which is coupled to T_1^0 will contribute positively to the D_{AB}. One way to assess these contributions is by diagonalising the matrix with only the relevant couplings, T_3^+ or S_3, and see how the energies of T_1^+ or T_1^0 are affected. The small bielectronic integrals δ_4 and δ_4' also allow the contribution of T_4^+ and S_4 but with a much smaller impact.

In the presence of an electric field applied in the Y direction, the situation of Table 4.1, the h_i and h_i' electronic coupling are no longer zero and new pathways open up for the DMI. As shown in matrix **??**, the d_z component is created by the coupling between the T_1^0 and the S_1 states which can be expressed using second-order pertubation theory:

$$\frac{id_z}{2} = \langle S|\, H^{SO}\, |T^0\rangle^{(0)} = \frac{\langle S_1|\, H^{SO}\, |T_2^0\rangle\, \langle T_2^0|\, H^{el}\, |T_1^0\rangle}{E_2+J_2-E_1} + \frac{\langle S_1|\, H^{el}\, |S_3\rangle\, \langle S_3|\, H^{SO}\, |T_1^0\rangle}{E_3-E_1} \tag{4.2.8}$$

This equation is only valid far from first order SOC regime but helps visualising how the DMI appears due to the combination of electronic and spin-orbit couplings.

For a full extraction, one must also consider the effect of higher lying states formed from determinants with the d_{xz} or d_{yz} orbitals, noted as $a_3(b_3)$ and $a_4(b_4)$, singly occupied.

$$
\begin{aligned}
T_5^+ &= \frac{-|a_1 b_3| + |b_1 a_3|}{\sqrt{2}} \qquad T_5^0 = \frac{-|a_1 \bar{b}_3| + |b_1 \bar{a}_3| - |a_3 \bar{b}_1| + |b_3 \bar{a}_1|}{2} \\
S_5 &= \frac{-|a_1 \bar{b}_4| + |b_1 \bar{a}_3| + |a_3 \bar{b}_1| - |b_3 \bar{a}_1|}{2} \\
T_6^+ &= \frac{-|a_1 b_4| + |b_1 a_4|}{\sqrt{2}} \qquad T_6^0 = \frac{-|a_1 \bar{b}_4| + |b_1 \bar{a}_4| - |a_4 \bar{b}_1| + |b_4 \bar{a}_1|}{2} \\
S_6 &= \frac{-|a_1 \bar{b}_4| + |b_1 \bar{a}_4| + |a_4 \bar{b}_1| - |b_4 \bar{a}_1|}{2}
\end{aligned}
\tag{4.2.9}
$$

These states are coupled with T_1 and S_1 through the $\hat{l}_+\hat{s}_- + \hat{l}_-\hat{s}_+$ operator in $\hat{H}^{SO}$. Note that the determinants formed from the d_{z^2} orbital can be omitted because it cannot interact with either T_1 or S_1 via $\hat{H}^{SO}$. Taking these states into account enable differentiation the two M_S=±1 of the triplet state and introduce rhombicity.

4.3 Impact of First Order Spin Orbit Coupling in the absence of electric field

Symmetric anisotropic exchange is described by a tensor of rank-two with six different components in a random set of axis. When expressed in its proper axis, it is reduced to simply two components, an axial parameter D_{AB} and rhombic term E_{AB}. Expressions for these terms have already been derived using second-order perturbation theory and involve the $T_5(S_5)$ and $T_6(S_6)$ states:

$$
\begin{aligned}
D_{AB} &= 4\frac{\zeta^2 J_3}{\Delta E_3^2} - \frac{1}{2}\left(\frac{\zeta^2 J_5}{\Delta E_5^2} + \frac{\zeta^2 J_6}{\Delta E_6^2}\right) \\
E_{AB} &= \frac{1}{2}\left(\frac{\zeta^2 J_5}{\Delta E_5^2} - \frac{\zeta^2 J_6}{\Delta E_6^2}\right)
\end{aligned}
\tag{4.3.1}
$$

where $\Delta E_i^2 = \sqrt{\Delta T_i \Delta S_i}$ is the geometric mean the of excitation energies between the states T_1 and T_i or S_i and $J_i = E_{T_i} - E_{S_i}$ is the isotropic coupling between excited states. As the first term of D_{AB} in eq 4.3.1 involves a state that contributes to 1^{st} order SOC, its estimation may deteriorate as ϕ decreases, *i.e* entering first order regime. This renders the equations valid only far from first-order regime and in the absence of external field. Note that the rhombic term requires the inclusion of the higher states for it to be different from zero.

Performing a rigorous extraction of the anisotropic parameter would require including all the excited states generated from single excitations within the d-orbital space, *i.e* CAS(18,10). As this work focus solely on the contribution of 1^{st} order SOC, a CAS(6,4) is sufficient. To assess the impact of dynamical correlation on the D_{AB} parameter, calculations were performed with gradual inclusion of the DDCI3 components (energy and wave-function). These results are reported on Figure 4.2 with the angle ϕ variating from 130° to 170°.

This shows that the magnitude $|D_{AB}|$ increases when entering 1^{st} order SOC, *i.e* a decrease of the angle ϕ. A similar observation has been made for the DMI in previous study and in mononuclear complexes for local ZFS parameter D. It is important to note that far from first-order SOC, the impact of electron correlation is minimal, with

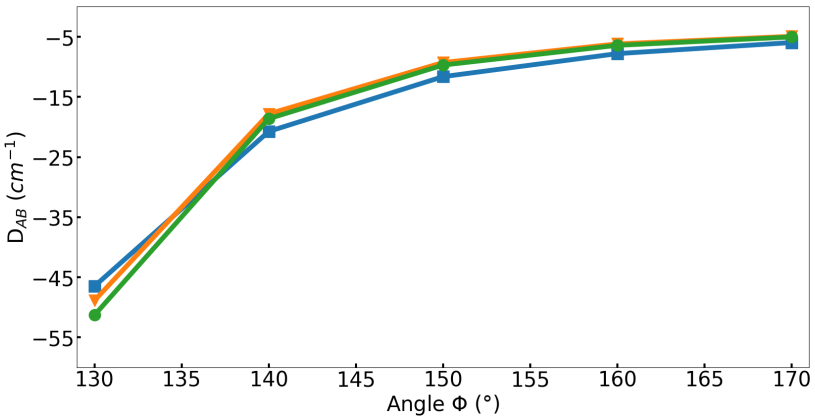

Figure 4.2: D_{AB} as a function of the outside angle ϕ for (i) CAS(6,4)SCF/SCF-SO level (blue line with squares), (ii) CAS(6,4)DDCI/SCF-SO level (orange line with triangles), and (iii) CAS(6,4)DDCI/DDCI-SO level (green line with circles)

only slight variations between the three curves. This difference increases as the angle ϕ decreases. It should be noted that the curves (ii) and (iii), which differ in terms of the wave-function used (CASSCF-SO or DDCI-SO) are very similar and that the inclusion of the DDCI wave-function does not improve the results much unlike what was observed with the DMI. Therefore, the use of the correlated DDCI wave-functions in addition to the DDCI energies is not required and CASSCF wave-function should suffice for the SO-SI calculation in the absence of DMI.

Far from first-order SOC limit, the equation 4.3.1 can be used with the large active space CAS(18,10) taking into account the states 4.2.9. At $\phi = 170°$, the perturbative espressions give D_{AB}^{pert}=-4.86cm^{-1} and E_{AB}^{pert}=0.18cm^{-1}, which is a good estimate when compared to the value extracted from the CAS(18,10)DDCI/DDCI-SO and effective Hamiltonian theory D_{AB}=-4.09cm^{-1} and E_{AB}=0.10cm^{-1}. The slight overestimation may be due to the fact that a unique $\zeta = 830cm^{-1}$ value of the free ion Cu^{2+} was used, in a complex this value is bound to decrease. As expected, these expressions lose their quality when entering first-order SOC, $\phi = 130°$, D_{AB}^{pert}=-83.31cm^{-1} and E_{AB}^{pert}=0.21cm^{-1} compared with the values extracted from CAS(18,10)DDCI/DDCI-SO and effective Hamiltonian theory D_{AB}=-45.20cm^{-1} and E_{AB}=0.02cm^{-1}. The rhombicity is negligible justifying the use of the smaller active space CAS(6,4) compared to the CAS(18,10).

$\hat{H}^{SO}$	$\|T_1^+\rangle$	$\|T_2^+\rangle$	$\|T_3^+\rangle$	$\|T_4^+\rangle$	$\|T_1^0\rangle$	$\|T_2^0\rangle$	$\|T_4^0\rangle$	$\|S_1\rangle$	$\|S_3\rangle$	$\|S_4\rangle$
$\langle T_1^+\|$	1585	0	1079i	12	0	0	0	0	0	0
$\langle T_2^+\|$	0	2362	0	0	0	0	0	0	0	0
$\langle T_3^+\|$	-1079i	0	3275	1079i	0	0	0	0	0	0
$\langle T_4^+\|$	12	0	-1079i	5036	0	0	0	0	0	0
$\langle T_1^0\|$	0	0	0	0	1585	0	12	0	-1078i	0
$\langle T_2^0\|$	0	0	0	0	0	2362	0	-1075i	0	-1076i
$\langle T_4^0\|$	0	0	0	0	12	0	5036	0	-1078i	0
$\langle S_1\|$	0	0	0	0	0	1075i	0	550	0	2
$\langle S_3\|$	0	0	0	0	1078i	0	1078i	0	3369	0
$\langle S_4\|$	0	0	0	0	0	1076i	0	2	0	4486

Table 4.2: Numerical matrix of $\hat{H}^{SO}$ and electronic couplings in the uncoupled basis from a CAS(6,4)DDCI/DDCI-SO calculation with no electric field and $\phi = 130°$.

	D_{AB}
Contribution of T_3^+ and T_3^-	-1176.74
Contribution of S_3	1124.28
Sum	-52.46
D_{AB} from H^{eff}	-52.46

Table 4.3: Variational contribution in cm^{-1} of the excited states to D_{AB} and its value in cm^{-1} extracted from effective Hamiltonian at CAS(6,4)DDCI/DDCI-SO level

The matrix 4.1 was extracted from *ab initio* CAS(6,4)DDCI/DCCI-SO calculation at $\phi = 130°$ and in the absence of an electrical field. Its numerical matrix is shown in Table 4.2, which shows a good correspondence. Note that the coupling terms h_i are equal to zero making it impossible for DMI to occur. Diagonalising this matrix with or without the inclusion of T_3^+ and S_3 allows to determine their individual contributions to the D_{AB}, which are reported in Table 4.3. The sum of these contributions matches perfectly with the value obtained via H^{eff}.

Note that from the final value of D_{AB} and the perturbative expression 4.3.1, it is clear that the main contribution to the D_AB comes from T_3 and S_3 even with the large active space CAS(18,10). This justify once more the use of the small CAS(6,4) calculations.

4.4 Impact of the electric field on the symmetric anisotropic exchange parameter

This section focuses on the bahaviour of the anisotropic parameter in first-order spin orbit coupling, at $\phi = 130°$, with the application of an external electric field. Only changes in the electronic structure are studied, not the geometric ones. Indeed a previous study showed that the geometric changes only affect the values of the parameters and not their physical origin.

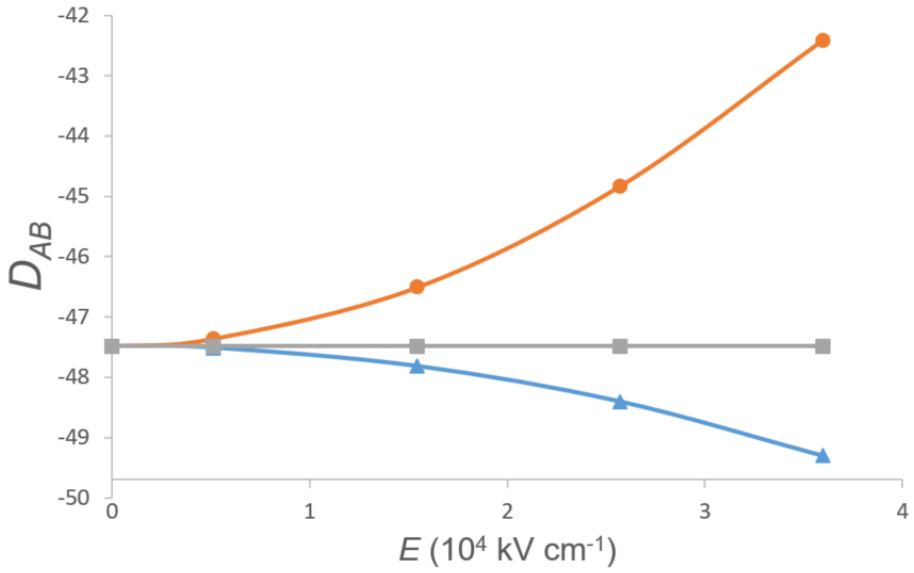

Figure 4.3: D_{AB} (in cm^{-1}) as a function of the electric field applied in the X (blue line with triangles), Y (red line with circles) and Z (grey line with squares) directions, obtained at CAS(6,4)SCF/SCF-SO

To obtain an initial estimate of the impact of the electric field on the D_{AB} parameter, CAS(6,4)SCF/SCF-SO calculations were performed with the electric field applied in the three cartesian directions (the axes are represented on Figure 4.1). The results are shown in Figure 4.3, a slight variation is observed when the electric field is applied along the X axis, but no change when it is applied along the Z direction. However, when the electric field is applied in the Y direction, a significant variation is observed. This behaviour was also observed in the study of the DMI where the largest value was obtained with the electic field along the Y direction. Therefore, this direction of application was chosen for further investigation as it showed the greater change in the two parameters. The impact of electron correlation is shown on Figure 4.4 with the evolution of the D_{AB} parameter under an electric field. It shows a large impact of both correlated energies and wave-functions as the field increases. The importance of dynamical correlation is expected, because as the field increases so does the DMI value making the use of DDCI energies and wave-function, *i.e* CAS(6,4)DDCI-DDCI-SO, mandatory as shown in previous studies.

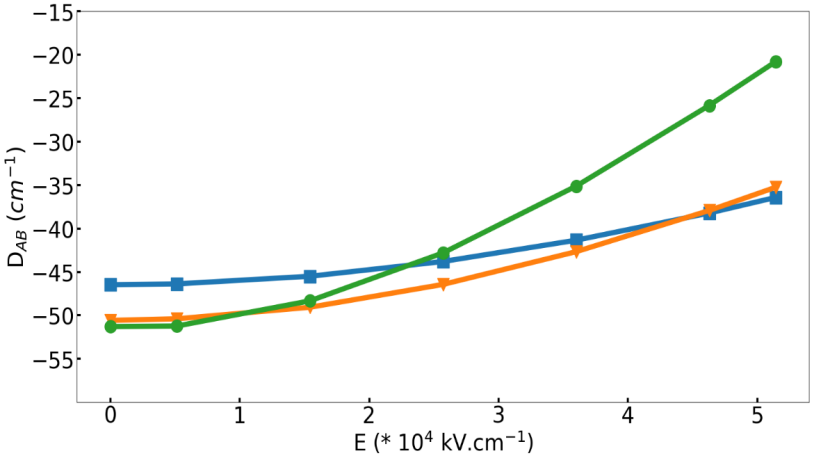

Figure 4.4: D_{AB} (in cm^{-1}) as a function of the electric field applied in the Y direction, obtained at (i)CAS(6,4)SCF/SCF-SO (blue line with squares), (ii) CAS(6,4)DDCI/SCF-SO (orange line with triangles) and (iii) CAS(6,4)DDCI/DDCI-SO (green line with circles)

Applying the electric field in the Y direction results in a decrease of the axial parameter magnitude $|D_{AB}|$. To identify the cause of this decrease, the numerical matrix 4.4 was extracted.

Note that now, the h_i terms are no longer zero, allowing DMI via the coupling from eq 4.2.8. The same diagonalisation procedure as in section 4.3 is applied, selecting states that may contribute to either the D_{AB} or the DMI. This enables the impact of the electric field on the axial parameter and its behaviour in the presence of DMI to be determined. The decomposition of the different contributions is reported in Table 4.5. The contributions from the $T_3^{\pm 1}$ and S_3 as well as the sum of the two, are comparable to the previous case in the absence of electric field. The effect of the electric field is mainly evident in the h_1 and h_1' terms, which couple the components of the T_1 and T_2 states, thereby enabling DMI to emerge. These two couplings have large contributions to the $|d_{AB}|$ term, accounting for 99% of the DMI parameter extracted from H^{eff}. On the other hand, these couplings have positive contributions to the D_{AB}, leading to a decrease in its magnitude $|D_{AB}|$ This demonstrates that there is an interferential

$\hat{H}^{SO}$	$\|T_1^+\rangle$	$\|T_2^+\rangle$	$\|T_3^+\rangle$	$\|T_4^+\rangle$	$\|T_1^0\rangle$	$\|T_2^0\rangle$	$\|T_4^0\rangle$	$\|S_1\rangle$	$\|S_3\rangle$	$\|S_4\rangle$
$\langle T_1^+\|$	1580	-201	1078i	12	0	0	0	0	0	0
$\langle T_2^+\|$	-201	2394	0	203	0	0	0	0	0	0
$\langle T_3^+\|$	-1078i	0	3294	1077i	0	0	0	0	0	0
$\langle T_4^+\|$	12	203	-1077i	5081	0	0	0	0	0	0
$\langle T_1^0\|$	0	0	0	0	1580	-201	12	0	-1078i	0
$\langle T_2^0\|$	0	0	0	0	-201	2394	203	-1075i	0	-1075i
$\langle T_4^0\|$	0	0	0	0	12	203	5081	0	-1077i	0
$\langle S_1\|$	0	0	0	0	0	1075i	0	556	202	1
$\langle S_3\|$	0	0	0	0	1078i	0	1077i	202	3369	-207
$\langle S_4\|$	0	0	0	0	0	1075i	0	1	-207	4541

Table 4.4: Numerical matrix of $\hat{H}^{SO}$ and electronic couplings in the uncoupled basis from a CAS(6,4)DDCI/DDCI-SO calculation in the presence of an electric field of 0.01 a.u (5.1724×10^4 kV.cm^{-1}) and $\phi = 130°$.

	D_{AB}	$\|d_{AB}\|$
Contribution of T_3^+ and T_3^-	-1162.0	0
Contribution of S_3	1111.4	0
Sum	-50.6	0
Contribution of h_1'	-7	-86.6
Contribution of h_1	29.3	329.7
Contribution of h_2'	5.9	29.1
Contribution of h_2	-0.4	-24.0
Total sum	-22.8	248.2
Parameters from H^{eff}	-21.03	245.0

Table 4.5: Variational contribution in cm^{-1} of the excited states to D_{AB} and $|d_{ab}|$ given in value in cm^{-1} extracted from effective Hamiltonian at CAS(6,4)DDCI/DDCI-SO level

behaviour between the two anisotropic parameters when the field is applied in the Y direction. This behaviour is not observed for other orientations. When the field is applied along the X direction, the D_{AB} term is affected (see Figure 4.3) while the d_{AB} remains zero as previously shown. Along the Z direction, it is the D_{AB} parameter that stays constant while a d_{AB} term can be observed, albeit much smaller.

4.4.1 Conclusion

This work studied the behaviour of the symmetric anisotropy parameters were studied in a binuclear Cu(II) complex, identifying different mechanisms as the source of their variations. The first part focused on the impact of first-order coupling on the axial D_{AB} and rhombic E_{AB} terms under certain geometry conditions. It showed that as the local environment of each metallic centreapproaches a C_3 symmetry, the condition for first-order coupling are met, allowing for large values of axial anisotropy. Initially, parameters were extracted perturbatively using previously derived expressions. However, this method of extraction proved to be no longer valid in first-order SOC regime and a variational approach was devised instead. This approach relies on the diagonalisation of the electronic and spin-orbit matrix in the basis of the three M_S components of the four triplet and four singlet states generated by a reduced active space consisting of the two highest d orbitals. In this first part, the importance of the use of dynamically correlated wave-function during the extraction was determined. It showed that in the absence of DMI terms, reasonnable values of the D_{AB} parameter can be obtained using the non-dynamically correlated CASSCF wave-function using corrected energies during the SO-SI step of the calculation. Once a DMI term appears, this is no longer true and the use of both the correlated energies and wave-function are necessary for a rigorous extraction. The second part introduces the application of an external electric field, focusing on its impact on the axial parameter. As with the DMI, it was demonstrated that the D_{AB} can also be influenced by an electric field and could contribute to the magneto-electric coupling. Three orientations of the electric field were explored and it was shown that, in one instance an interferential behaviour could be observed between the D_{AB} and d_{AB} terms. Analysis of the numerical matrices showed that the coupling at the DMI source for this field orientation also impacted the magnitude of the axial parameter: when the former increased, the latter decreased.

This work complements a series of studies attempting to define a recipe for obtaining large values for the parameters of both types of anisotropy (symmetric and antisymmetric). Two key elements have been identified as necessary in order to obtain such results.

(i) geometries around the metal must allow the near-degeneracy of d-orbitals to approach first-order SOC. This can be achieved with geometries containing symmetries such as a C_3 axis.

(ii) hybdridisation of the degenerate orbitals must be possible via the application an electric field. The choice of orientation of the field leads different type of hybdridisation due to the deformation of the electronic could.

These considerations could pave the way for the design of compounds with strong magneto-electric coupling.

Chapter 5

Herbertsmithite

Computational Informations

The structure studied was taken from a X-ray study, the Hydrogen position were optimised using periodic DFT with PBE functional implemented in the Quantum Espresso code.

Density functional theory calculations were performed using the ORCA package with def2-TZVP basis set on all atoms and the ωB97X-D3 functional which has shown to provide very good value of magnetic couplings. Wave-function based method calculations were carried out with the MOLCAS and CASDI codes with the extended ANO-RCC basis set (6s5p3d2f for Cu and Zn, 4s3p2d for O, 4s3p1d for Cl and 2s1p for H)

The embedding's pseudopotential were set to the SDD Effective Core Potentiel (ECP) for ORCA calculations and *ab initio* model potentials (AIMP) for MOLCAS calculations. The quality of the embedding was checked by comparing the value of J_1 using the B3LYP functional for embedded cluster and periodic calculations (using the Crystal code). The J1 values are in perfect agreement: 240K for periodic and 239K for embedded cluster. As we will see below, these B3LYP values slightly overestimate the coupling but demonstrate the adequacy of the material model adopted in this study.

5.1 Density-Functional Theory study

In a first approximation, the isotropic behavior of Herbertsmithite is described by an unique first neighbor coupling. The highly-correlated nature of such system suggests the possibility of longer range interaction between copper ions separated by one or more neighbors. To explore this possibility, the need to compute large fragments arises making the application of wave-function based method complicated. First the number of Cu^{2+} into the fragment has a direct impact on the size of the active space, even restricting to one orbital/one electron per copper centres leads to convergence troubles in the calculations. Also, the number of determinant and spin states generated prohibits the use of Post-CASSCF methods which are crucial for a good estimation of magnetic couplings. Finally, the number of spin states render the analytical derivation complicated with large matrices to diagonalize. As such, Density Functional Theory provides a good middle ground to compute large systems. It also presents some disadvantages, the DFT wave-function is monodeterminantal and usually not an eigenfunction of the $\hat{S}^2$ operator which prevents the mapping on the HDvV Hamiltonian. Nevertheless, the combinated use of Broken-Symmetry DFT (BS-DFT) and the Ising Hamiltonian provides a good way to obtain an estimation of the couplings in the system. The Broken-

Symmetry approach relies on the computation of DFT solutions where the M_S value of spin moment of each copper ion of the fragment have been imposed beforehand to $\pm\frac{1}{2}$. It is then possible to obtain multiple solutions per fragments to make a connection between the energy differenceés of each solution and the Ising Hamiltonian energies. Additionaly, the time necessary for a DFT calculation and for the derivation of its analytical solution allows for the exploration of different properties of the embedding such as the size of the fragments and its overall quality.

In-plane couplings

In a first description, a fragment presenting only the first neighbor coupling was introduced with three copper ions as shown on Figure 5.1(a). Four solutions can be computed with $M_S \geq 0$, first a $M_S = 3/2$ where all magnetic moment of the Cu^{2+} ions are aligned creating a fully ferromagnetic solution. Then, three other solutions are possible by switching the M_S value of one of the Cu^{2+} ion to $-1/2$. If the choice of fragment and construction of the embedding are done correctly, this should lead to three equal energy differences as these solutions are degenerate in the Ising Hamiltonian.

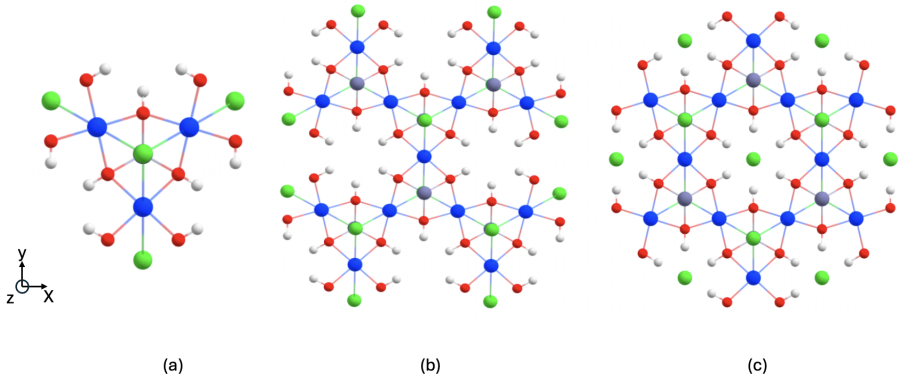

Figure 5.1: Fragments considred for DFT calculations for in plane component, (a) trimer (b) 13Cu (c)12Cu

Let us call the highest occupied orbital of each copper ion a, b and c. The Slater determinant describing the high spin solution (M_S=+1/2 on each Cu^{2+}) can then be written $|abc|$ while the low spin solutions (one of the M_S value is switched to $-1/2$) are written $|ab\bar{c}|$,$|a\bar{b}c|$ and $|\bar{a}bc|$. Applying $\hat{H}_{Ising} = \sum_{i,j} J_1 \hat{S}_{i,z}\hat{S}_{j,z}$ to the high spin (HS) solution $|abc|$ gives the eigenvalue $\frac{3}{2}J_1$ while the application on the low spin (LS) solutions gives the eigenvalue $\frac{1}{2}J_1$. The Ising Hamiltonian's matrix representation is diagonal:

H_{Ising}	$\|abc\|$	$\|ab\bar{c}\|$	$\|a\bar{b}c\|$	$\|\bar{a}bc\|$
$\|abc\|$	$\frac{3}{2}J_1$	0	0	0
$\|ab\bar{c}\|$	0	$\frac{1}{2}J_1$	0	0
$\|a\bar{b}c\|$	0	0	$\frac{1}{2}J_1$	0
$\|\bar{a}bc\|$	0	0	0	$\frac{1}{2}J_1$

The value of J_1 can then be extracted from the difference in energy between the high spin solution and low-spin ones:

$$J_1 = E_{HS} - E_{LS} \tag{5.1.1}$$

The same procedure of extraction can now be applied to largers fragment allowing the introduction of longer range couplings. The second fragment created included nine copper ions which allows for the consideration of two new couplings, J_2 and J_3 represented on Figure 5.2. It indicated that these couplings were small ($|J_2| \approx |J_3| \approx 1cm^{-1}$ each) with a large standard deviation. While these results provided good insight on the nature of these two couplings, the extraction was unsatisfactory. The source of this deviation is believed to be the environment of ions taking part in the interaction. The extraction of these couplings requires to to flip the spin of at least one of the ion at the edge of the fragment whose neighboring atoms are not always explicitely computed (treated with ECP's). It was decided to increase the size of the fragment to twelve and thirteen copper ions (fragment (c) and (b) from Figure 5.1) so that there would be ways account for these interaction within the centreof the fragments.

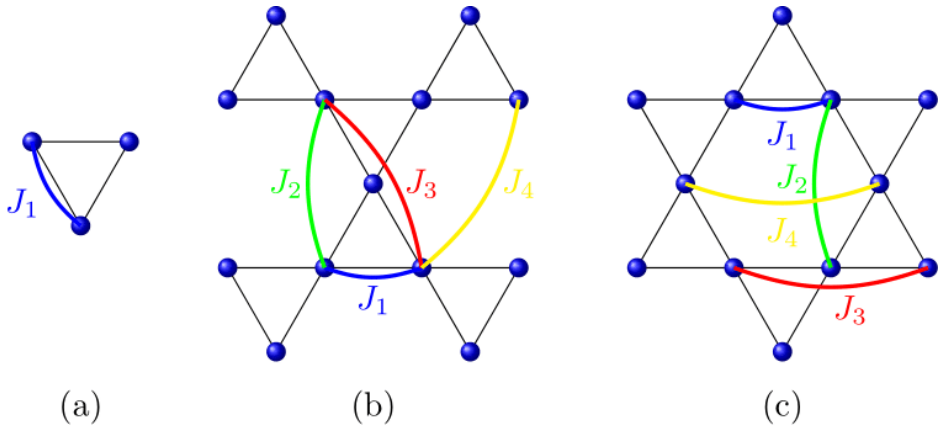

Figure 5.2: Schematic representation of the fragments and the couplings introduced

The results obtained for each couplings in the thre fragments are presented in Table 5.1. The first thing to note is the good transferability with a small relative deviation from one cluster to the other. Note that with this convention of the Ising Hamiltonian (a plus sign in front of the J term), a positive value indicates antiferromagnetism while negative indicates ferromagnetism. The closest neighbor interaction J_1 is in good agreement with values published in the litterature while J_2,J_3 and J_4 are very weak.

$J_i(K)$	(a)	(b)	(c)	d_{Cu-Cu} (Å)
J_1	178.0	191.2	181.0	3.42
J_2	-	0.5	0.4	5.91
J_3	-	-1.1	-1.0	6.83
J_4	-	-0.1	-0.2	6.83

These results highlight the mainly antiferromagnetic nature of these interactions with a leading interaction J_1 at least two order of magnitude higher than the other. This confirm the the use of models composed of only one J interaction, the negligenge of other couplings should cause no more than a small deviation.

Out-of-plane coupling

Another preoccupation of the model is the occupation disorder. Cristallographic studies have identified two types of defect present at low temperatures. The first is the substitution of the Zn^{2+} inter-plane site with a Cu^{2+} ion, estimated to occur at a

rate of 0.15, and the second is a Zn^{2+} ion entering the Kagome plane with a much smaller occurance rate (<0.05). Following the same approach, an embedding with the defect at its centre was constructed to include the inter-ion, the fragment is shown in Figure 5.3. This contains two layers of Kagome planes, each with three Cu^{2+} ions and their neighbouring ions while the interstitial Zn^{2+} ion is replaced by a copper ion. In a structuraly perfect Kagome lattice, the inter*-site is occupied by a Zn^{2+} ion which is not susceptible to the Jahn-Teller effect because of its doubly occupied d-orbitals, allowing for a C_3 symmetry axis. However, replacing this ion with a Cu^{2+}, which is susceptible to the Jahn-Teller effect with a singly occupied d-orbital, induces structural deformation in the vicinity of the defect.

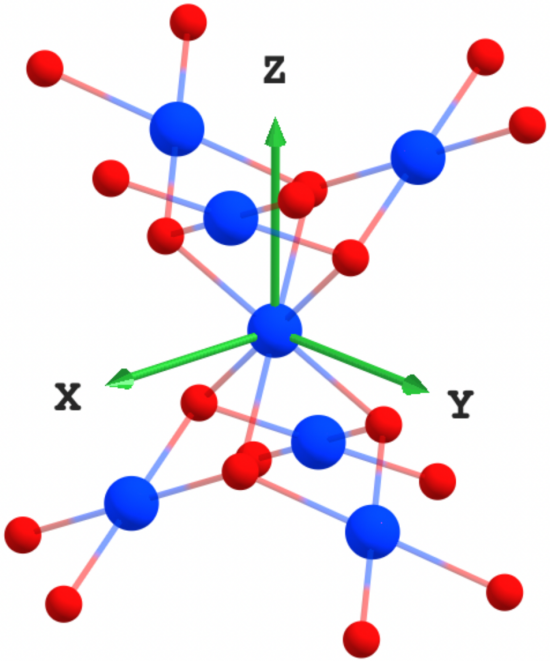

Figure 5.3: Embedded cluster used to compute the out of plane coupling before geometry optimisation. The three copper ions (blue) at the top and bottom of the fragment each belong to their own kagome plane.

To account for the deformations, the structure of the fragment was optimised using the ORCA package via DFT calculations with the PBE or B3LYP functionals. It is expected that local impurities act only locally and should not have any long range effect, thus no changes were made to the embedding. To order to maintain the rigidity of the crystal structure only the coordination sphere, *i.e* the hydroxide groups close to the defect, was left free during optimisation, while the positions of the remaining ions were constrained. Depending on the functional used, two different types of structure were obtained. The PBE functional calculation converges towards a structure with four short Cu-O bonds and two long ones, this structure is referred to as the "4+2" structure. While the B3LYP functional calculation converges towards the opposite, with two short Cu-O bonds and four long ones. This structure is labelled "2+4". In order to determine the most sTable structure, one would compare the final single-point energy provided by the program at the end of the *SCF* cycle. However, comparing energies obtained using different functionals is not appropriate. Therefore, a second set of optimisations was performed starting from the previously obtained PBE (B3LYP) structure but now using the B3LYP (PBE) functional. Both calculations converged towards the "4+2"

structure which was found to be slightly lower in energy than the "2+4" structure with a difference of $\Delta E = 100K$ using the B3LYP functional. As the two structures are quite close in energy, a difference lower than the estimated first neighbour coupling, both structures were explored for the extraction of J couplings.

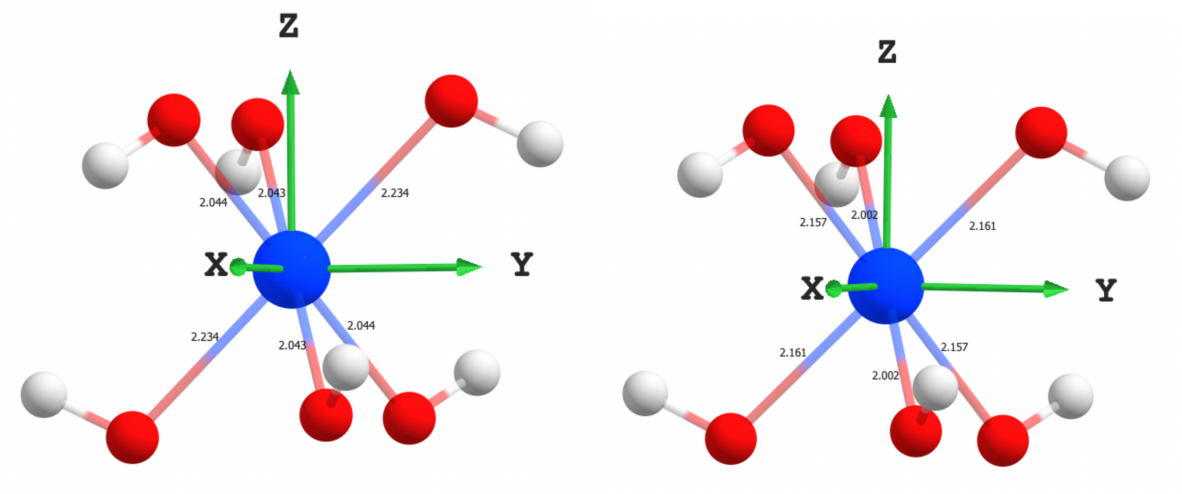

(a) "4+2" structure (b) "2+4" structure

Figure 5.4: Close environment of intersite Cu^{2+} in both structure obtained via DFT with the B3LYP functional. The bond lengths are shown in Angstrom

These distortions, together with the presence of a copper ion at the intersite, require the definition of new J_i couplings. Table 5.1 shows the distances between the oxygens atoms and the different Cu^{2+} ions. In both the optimised structures, one type of oxygens moves away from the in-plane copper while the other moves closer.

	X-ray	"4+2"	"2+4"
$Cu_{defect} - O$ (1)	2.11887	2.04391	2.16123
$Cu_{defect} - O$ (2)	"	2.23438	2.00165
$Cu_{plane} - O(1)$	1.98423	2.01279	1.9882
$Cu_{plane} - O(2)$	"	1.97252	2.03068

Table 5.1: Distance between the oxygens and the copper ions, defect or in plane, given in Åfor the X-Ray structure and both optimisation scheme.

This displacement results to a second in-plane coupling J_1', which differs from the J_1 by the distance between the copper ions and the bridging oxygen. Focusing on a triad of $Cu2+$ ions in the same plane, two bridging oxygens occupy equivalent positions while the third one occupies a different position. The J_1 coupling is defined between two $Cu2+$ ions bridged by one of the two equivalent oxygens for a total of two J_1 couplings in the triad while J_1' denotes the final possible coupling. The out-of-plane coupling is a bit more complicated as the two copper ions involved are bridged by two oxygens. The coupling between two Cu_{2+} bridged by two equivalent oxygens is called J_5 and appears once in the triad involving the defect. The coupling going through two non-equivalent bridges, in turn, is referred to as J_5', this coupling appears twice in the triad.

Table 5.2 shows the values extracted using BS-DFT for both the optimised and C_3 structure for comparison. The C_3 structure indicates a strong J_1 antiferromagnetic coupling which is consistent with previously extracted values, as well as a non negligible

J_i (K)	J_1	J'_1	J_5	J'_5
$Xray$	184.22		-80,64	
"4+2"	92.9	262.9	-47.5	-73.0
"2+4"	185.3	66.14	-81.61	-63.4

Table 5.2: Values of the J_i in Kelvin interactions in presence of a Cu^{2+} defect in the intersite.

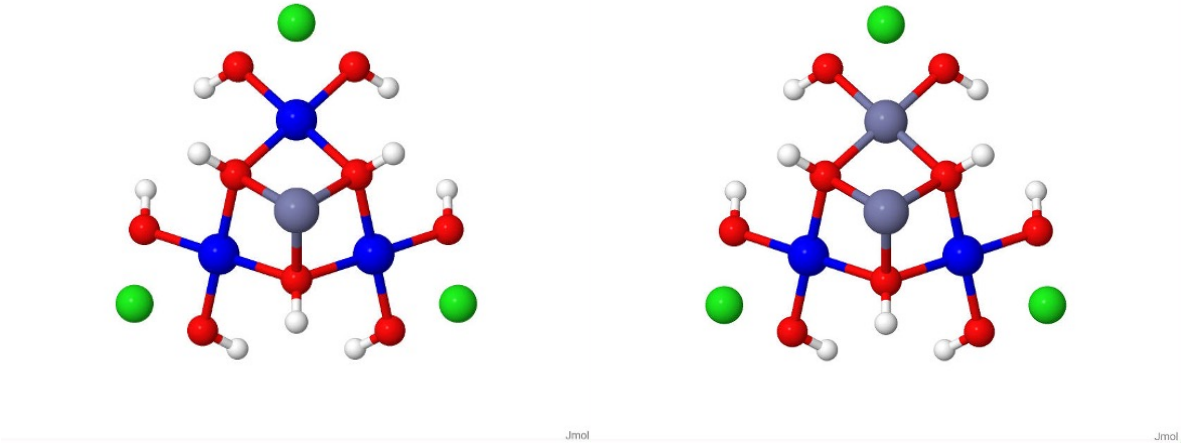

(a) Trimer (b) Dimer

Figure 5.5: Embedded clusters used for Wave-funciton computation

out-of-plane ferromagnetic coupling J_5. Extractions from the optimised structure show a significant impact of the deformations on the first neighbor coupling. Firstly, coupling withing the plane decreases as oxygen atoms move away from it, whereas it increases as they move closer. This is not surprising, since the hopping term involved in the antiferromagnetic contribution of superexchange is sensitive to distance. Note that these displacements lead to significant differences in the values of couplings of the same nature. The most important result of this study is the identification of a ferromagnetic coupling between the in-plane copper ion and the defects.

5.2 Wave-Function Theory study

A second purpose of this study was the determination of anisotropic interaction in the crystal. The extraction of such interactions follows the same procedure as described in chapter chapter 4. The computation of SO-states being very computationally demanding, this extraction will be resticted to two fragments of small size.

The first fragment, Figure 5.5a, is similar to the one used for DFT calculation, with three copper ions arranged in an equilateral triangle. A second fragment 5.5b was designed by substituting one of the Cu^{2+} with a diamagnetic Zn^{2+}, both share rather close structural properties (charge, mass, ionic radius). As the d shell of the zinc ion is completely filled it will not take part in the magnetic interactions, leaving us with essentially a dimer to capture the interaction of only two Cu^{2+}. This approach has been studied in serveral other materials and we will see from the results that this substitution has little impact on the extracted values but can significally reduce ther overall study time.

5.2.1 Isotropic Coupling

To check the applicability of WFT calculation to this system, the first step was to try and reproduce the J_1 value. In both cluster, two type of active space were considered:

- one electron and orbital per magnetic center.
- all eletrons occupying the d shell of each magnetic center.

The first type of active space results in a CAS(2,2) for the dimer calculation which generates one triplet (S=1) and one singlet (S=0) state.

$$|1,1\rangle = |ab| \tag{5.2.1}$$

$$|1,0\rangle = \frac{1}{\sqrt{2}}(|a\bar{b}| - |b\bar{a}|) \tag{5.2.2}$$

$$|1,-1\rangle = |\bar{a}\bar{b}| \tag{5.2.3}$$

$$|0,0\rangle = \frac{1}{\sqrt{2}}(|a\bar{b}| + |b\bar{a}|) \tag{5.2.4}$$

The value of J_1 is then given by the difference in energy between the triplet and singlet state $J_1 = E(S=1) - E(S=0)$. The enlarged active space CAS(18,10) generates 25 Triplet and 25 Singlet states.

In the case of the trimer cluster, CAS(3,3) represents the minimum active space which generates 1 quartet (S=3/2) state and two doublet (S=1/2) states. The two doublet are degenerate if only one value of J is taken into account as is our case with an equilateral repartition of the copper ions.

$$|3/2,3/2\rangle = |abc| \tag{5.2.5}$$

$$|3/2,1/2\rangle = \frac{1}{\sqrt{3}}(|ab\bar{c}| + |a\bar{b}c| + |\bar{a}bc|) \tag{5.2.6}$$

$$|1/2,1/2\rangle_1 = \frac{1}{\sqrt{6}}(|ab\bar{c}| + |a\bar{b}c| - 2|\bar{a}bc|) \tag{5.2.7}$$

$$|1/2,1/2\rangle_2 = \frac{1}{\sqrt{2}}(|ab\bar{c}| - |a\bar{b}c|) \tag{5.2.8}$$

The expression of the m_s component with negative value were left out as they only differ by the number of up and down spins. The value of J_1 is then given by $J_1 = \frac{2}{3}(E(S=3/2) - E(S=1/2))$. The enlarges active space CAS(27,15) generates 125 Quartet and 250 Doublets states.

CASSCF calculation tends to "over"-localise the wave-function on the metallic center, thus underestimating mechanism at the origing of the antiferromagnetic contribution to the J integral. As such it does not provides a good estimate but can nonetheless give informations about the nature of the coupling. Table 5.2.1 shows the results obtained at multiple level of calculation for different active space.

$J_1(K)$	CAS(2,2) CAS(3,3)	CAS(18,10) CAS(27,15)	CASPT2	DDCI1	DDCI3
Dimer	10.7	8.3	69.8	50.0	80.1
Trimer	8.2	7.7	56.0	50.7	60

These results indicate an antiferromagnetic J coupling with a large impact of dynamical correlation, yet these values do not match with the DFT calculations and the litterature.

An active space only composed of d-orbitals is not enough to achieve a correct estimation of the isotropic coupling in this system, to improve the description of the antiferromagnetic mechanisms it was then thought to bring the bridging ligand orbitals into the active space. The inclusion of the p-orbitals of the bridging oxygen presents a challenge, as they stay doubly occupied and do not contribute to the wave-function at CAS level, reaching a sTable active space becomes challenging because of convergence issue. To avoid these troubles, a methodology based on the projection of the oxygen's p-orbitals onto the ligand's tail of the active orbitals was applied. This allows to obtain a reproducible active space with well defined orbitals represented on Figure **??**.

It has been previously established that performing a DDCI1 calculation on a active space composed of the ligands orbitals in addition to the magnetic orbitals allows to obtain value of J coupling on par to a DDCI3 calculation. This allows to greatly reduce computational time, the active space is now composed of one electron/orbital per metallic centreand two electrons in one orbital per oxygen (CAS(4,3) in the dinuclear and CAS(9,6) in the trinuclear fragment). This procedure has allowed the extraction of new values for J_1 in both fragment, $J_1 = 105.3cm^{-1}$ in the dinuclear cluster and $J_1 = 126.3cm^{-1}$ in the trinuclear cluster. Even if the dinuclear value of J_1 is lower, the coupling extracted from the trinuclear fragment is well within range of the expected value by both DFT and experiment.

5.2.2 Anisotropic interactions

The computation of the isotropic couplings was a way to assertain the validity of our methods and calibration of the embedded cluster method. The electronic structure of the compound seems to be well replicated with a satisfying extraction of the these coupling. The main purpose of this study can now be adressed, which is the extraction of anisotropic interactions. Theoretical model propose the inclusion of a weak Dzyaloshinskii-Moriya pseudo-vector along the out of plane direction to account for the behavior at low temperature but the symmetric tensor of anisotropy $\overline{\overline{D}}_{ij}$ is usually left out. Following the procedure explained in 4, all three components of the DMI were extracted as well as the D_{ij}-tensor.

Bi-nuclear calculation

Starting from the CASSCF wave-function with the enlarge active space of all 18 copper d-shell electrons and the 10 d-orbitals, computation of the SO-states was performed using the SO-RASSI method implemented in MOLCAS. The lowest part of the energy spectrum was corrected using the isotropic coupling value previously obtained. No assumption on the magnetic axes were made and so the extraction of all anisotropic parameters (9 in total) was performed using effective hamiltonian theory with a model space composed of the three M_S component of the triplet state and the singlet state. The matrix representation of the model Hamiltonian in the model space basis is:

H_{MS}	$\lvert 1,-1\rangle$	$\lvert 1,0\rangle$	$\lvert 1,1\rangle$	$\lvert 0,0\rangle$
$\langle 1,-1\rvert$	$\frac{J}{4}+\frac{D_{zz}}{4}$	$\frac{D_{xz}-iD_{yz}}{2\sqrt{2}}$	$\frac{(D_{xx}-D_{zz}-2iD_{xy})}{4}$	$\frac{d_y+id_x}{2\sqrt{2}}$
$\langle 1,0\rvert$	$\frac{D_{xz}+iD_{yz}}{2\sqrt{2}}$	$\frac{J}{4}-\frac{D_{zz}}{4}+\frac{(D_{xx}+D_{yy})}{4}$	$-\frac{D_{xz}-iD_{yz}}{2\sqrt{2}}$	$-\frac{id_z}{2}$
$\langle 1,1\rvert$	$\frac{(D_{xx}-D_{zz}+2iD_{xy})}{4}$	$-\frac{D_{xz}+iD_{yz}}{2\sqrt{2}}$	$\frac{J}{4}+\frac{D_{zz}}{4}$	$\frac{d_y-id_x}{2\sqrt{2}}$
$\langle 0,0\rvert$	$\frac{d_y-id_x}{2\sqrt{2}}$	$\frac{id_z}{2}$	$\frac{d_y+id_x}{2\sqrt{2}}$	$-\frac{3J}{4}-\frac{D_{zz}}{4}-\frac{(D_{xx}+D_{yy})}{4}$

The values obtained for both interaction expressed in Kelvin in the axis system of the cluster are:

$$\overline{\overline{D}}_{12} = \begin{pmatrix} 1 & 0 & 0 \\ 0 & 1 & 0 \\ 0 & 0 & 1 \end{pmatrix} \qquad \mathbf{d}_{12} = \begin{pmatrix} 0 \\ 4.73 \\ 1.70 \end{pmatrix}$$

The symmetric tensor can be diagonalized to extract the $D = -0.46K$ axial parameter and a small $E = 0.13K$ rhombic term. These values are small and should have only little impact on the magnetic properties of this system however the DMI components are non negligible. The DMI value along the x-axis is naught, as expected from symmetry reason. Note that the in-plane component (along the y-axis) is larger than the out of plane component (along the z-axis), this result can be suprising but can be rationalized looking at the origins of the DMI component. It was demonstrated analyticaly that the DM-interaction comes from the hybdridization of the metal's d-orbitals. It showed that:

- a mixing between $d_{x^2-y^2}$ and d_{yz} or d_{xy} and d_{xz} generates a d_x component.
- a mixing between $d_{x^2-y^2}$ and d_{xz} or d_{xy} and d_{yz} generates a d_y component.
- a mixing between $d_{x^2-y^2}$ and d_{xy} or d_{xz} and d_{yz} generates a d_z component.

This mixing can be clearly observed on Figure 5.6, and from the expression of one of these magnetic orbitals on the Cartesian d-orbitals of one copper ion : $0.4889d_{x^2-y^2} + 0.2120d_{xz} - 0.2841d_{xy} - 0.3666d_{yz}$.

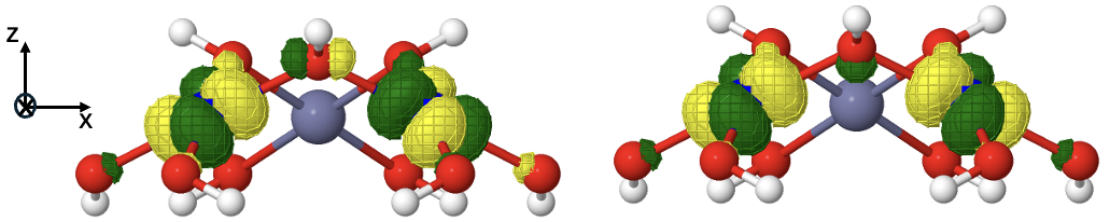

Figure 5.6: CAS(2,2)SCF magnetic orbitals calculated on the dimer fragment

Different configuration for the dimer cluster were explored to make sure the values extracted were not affected by which "couple" of Cu^{2+} ions were chosen. The extra zinc ion was swapped around all three in plane site followed by the same procedure of extraction. The same out of plane $|d_\perp|$ value and the same projection in the xy plane ($|d_\parallel|$) were found in all three calculations.

Trinuclear calculations

The extraction was then performed on the tri-nuclear fragment with an active space of 27 electrons in 15 orbitals. In the case of three magnetic center, the model Hamiltonian is now written:

$$\begin{aligned}\hat{H}_{MS} =& J_{12}\hat{\mathbf{S}}_1 \cdot \hat{\mathbf{S}}_2 + \hat{\mathbf{S}}_1 \cdot \overline{\overline{D}}_{12} \cdot \hat{\mathbf{S}}_2 + \mathbf{d}_{12} \cdot (\hat{\mathbf{S}}_1 \times \hat{\mathbf{S}}_2) \\ & J_{12}\hat{\mathbf{S}}_2 \cdot \hat{\mathbf{S}}_3 + \hat{\mathbf{S}}_2 \cdot \overline{\overline{D}}_{23} \cdot \hat{\mathbf{S}}_3 + \mathbf{d}_{23} \cdot (\hat{\mathbf{S}}_2 \times \hat{\mathbf{S}}_3) \\ & J_{13}\hat{\mathbf{S}}_1 \cdot \hat{\mathbf{S}}_3 + \hat{\mathbf{S}}_1 \cdot \overline{\overline{D}}_{13} \cdot \hat{\mathbf{S}}_3 - \mathbf{d}_{13} \cdot (\hat{\mathbf{S}}_1 \times \hat{\mathbf{S}}_3)\end{aligned} \tag{5.2.9}$$

Note the negative sing in front of the last term d_{13} which originates from the permutation realtionship specific to the DMI (d_{13}=-d_{31}). On the other hand we set $J_{12} = J_{23} = J_{13}$ and let the D_{ij}-tensor be expressed in the axis system of the cluster with 6 paramaters each. First, we can obtain the matrix representation of this Hamiltonian in the basis of the determinant formed from the three magnetic orbitals on each site (a, b and c) located on each copper center:

To express this matrix in the coupled basis, *i.e* in the basis formed from the m_s components of the quartet and two doublet states, one has to build the transofrmation matrix. This matrix can be obtained using the Clebsch-Gordan coefficients or by diagonalizing the HDvV Hamiltonian representation matrix and using the eigenvectors as the transition matrix.

U	$\lvert\frac{3}{2},\frac{3}{2}\rangle$	$\lvert\frac{3}{2},\frac{1}{2}\rangle$	$\lvert\frac{3}{2},-\frac{1}{2}\rangle$	$\lvert\frac{3}{2},\frac{3}{2}\rangle$	$\lvert\frac{1}{2},\frac{1}{2}\rangle_1$	$\lvert\frac{1}{2},-\frac{1}{2}\rangle_1$	$\lvert\frac{1}{2},\frac{1}{2}\rangle_2$	$\lvert\frac{1}{2},-\frac{1}{2}\rangle_2$
$\langle abc\rvert$	1	0	0	0	0	0	0	0
$\langle ab\bar{c}\rvert$	0	$\frac{1}{\sqrt{3}}$	0	0	0	0	$-\frac{2}{\sqrt{6}}$	0
$\langle a\bar{b}c\rvert$	0	$\frac{1}{\sqrt{3}}$	0	0	$-\frac{1}{\sqrt{2}}$	0	$\frac{1}{\sqrt{6}}$	0
$\langle \bar{a}bc\rvert$	0	$\frac{1}{\sqrt{3}}$	0	0	$\frac{1}{\sqrt{2}}$	0	$\frac{1}{\sqrt{6}}$	0
$\langle a\bar{b}\bar{c}\rvert$	0	0	$\frac{1}{\sqrt{3}}$	0	0	0	0	$-\frac{2}{\sqrt{6}}$
$\langle \bar{a}b\bar{c}\rvert$	0	0	$\frac{1}{\sqrt{3}}$	0	0	$-\frac{1}{\sqrt{2}}$	0	$\frac{1}{\sqrt{6}}$
$\langle \bar{a}\bar{b}c\rvert$	0	0	$\frac{1}{\sqrt{3}}$	0	0	$\frac{1}{\sqrt{2}}$	0	$\frac{1}{\sqrt{6}}$
$\langle \bar{a}\bar{b}\bar{c}\rvert$	0	0	0	1	0	0	0	0

	$\|Q^{3/2}_{3}\rangle$	$\|Q^{3/2}_{1}\rangle$	$\|Q^{1/2}_{2}\rangle$	$\|Q^{3/2}_{-1}\rangle$	$\|D^{1/2}_{1}\rangle$	$\|D^{1/2}_{-1}\rangle$	$\|D^{1/2}_{2}\rangle$	$\|D^{1/2}_{-2}\rangle$
$\|Q^{3/2}_{3}\rangle$	$\frac{3J}{4}$	0	0	0	$-\frac{\sqrt{2}}{8}i(2\boldsymbol{d}^{12}-\boldsymbol{d}^{13}-\boldsymbol{d}^{23})(\boldsymbol{e}_x+i\boldsymbol{e}_y)$	0	$\frac{\sqrt{6}}{8}(\boldsymbol{d}^{13}-\boldsymbol{d}^{23})(\boldsymbol{e}_x+i\boldsymbol{e}_y)$	0
$\|Q^{1/2}_{2}\rangle$	0	$\frac{3J}{4}$	0	0	$-\frac{i\sqrt{6}}{12}\boldsymbol{e}_z(2\boldsymbol{d}^{12}-\boldsymbol{d}^{13}-\boldsymbol{d}^{23})$	$-\frac{\sqrt{6}}{24}i(2\boldsymbol{d}^{12}-\boldsymbol{d}^{13}-\boldsymbol{d}^{13})(\boldsymbol{e}_x-i\boldsymbol{e}_y)$	$\frac{\sqrt{2}}{4}((\boldsymbol{d}^{13}-\boldsymbol{d}^{23})$	$\frac{\sqrt{2}}{8}((\boldsymbol{d}^{13}-\boldsymbol{d}^{23})(\boldsymbol{e}_x+i\boldsymbol{e}_y)$
$\|Q^{1/2}_{-2}\rangle$	0	0	$\frac{3J}{4}$	0	$\frac{\sqrt{6}}{24}i(2\boldsymbol{d}^{12}-\boldsymbol{d}^{13}-\boldsymbol{d}^{13})(\boldsymbol{e}_x-i\boldsymbol{e}_y)$	$-\frac{i\sqrt{6}}{12}\boldsymbol{e}_z(2\boldsymbol{d}^{12}-\boldsymbol{d}^{13}-\boldsymbol{d}^{23})$	$-\frac{\sqrt{2}}{8}((\boldsymbol{d}^{13}-\boldsymbol{d}^{23})(\boldsymbol{e}_x-i\boldsymbol{e}_y)$	$\frac{\sqrt{2}}{4}((\boldsymbol{d}^{13}-\boldsymbol{d}^{23})$
$\|Q^{3/2}_{-3}\rangle$	0	0	0	$\frac{3J}{4}$	0	$\frac{\sqrt{2}}{8}(2\boldsymbol{d}^{12}-\boldsymbol{d}^{13}-\boldsymbol{d}^{23})(\boldsymbol{e}_x+i\boldsymbol{e}_y)$	0	$-\frac{\sqrt{6}}{8}i(\boldsymbol{d}^{13}-\boldsymbol{d}^{23})(\boldsymbol{e}_x-i\boldsymbol{e}_y)$
$\|D^{1/2}_{1}\rangle$	0	0	0	0	$-\frac{3J}{4}$	0	$\frac{\sqrt{3}}{6}i(\boldsymbol{d}^{12}+\boldsymbol{d}^{13}+\boldsymbol{d}^{23})\boldsymbol{e}_z$	$-\frac{1}{2\sqrt{3}}i((\boldsymbol{d}^{12}+\boldsymbol{d}^{13}+\boldsymbol{d}^{23})(\boldsymbol{e}_x+i\boldsymbol{e}_y)$
$\|D^{1/2}_{-1}\rangle$	0	0	0	0	0	$-\frac{3J}{4}$	$-\frac{1}{2\sqrt{3}}i(\boldsymbol{d}^{12}+\boldsymbol{d}^{13}+\boldsymbol{d}^{23})(\boldsymbol{e}_x-i\boldsymbol{e}_y)$	$-\frac{1}{2\sqrt{3}}i\boldsymbol{e}_z(\boldsymbol{d}^{12}+\boldsymbol{d}^{13}+\boldsymbol{d}^{23})$
$\|D^{1/2}_{2}\rangle$	0	0	0	0	0	0	$-\frac{3J}{4}$	0
$\|D^{1/2}_{2}\rangle$	0	0	0	0	0	0	0	$-\frac{3J}{4}$

Figure 5.7: Representation matrix of the Multi-Spin Hamiltonian in the basis of the four components of the quartet and the doubly-degenerate doublet states

The symmetric tensor terms (6 each, 18 total) are left out of the matrix for clarity but are taken into account during the extraction. The extracted Dzyaloshinskii-Moriya pseudo vectors are:

$$\mathbf{d}_{12} = \begin{pmatrix} -4.1 \\ 2.36 \\ 1.70 \end{pmatrix} \qquad \mathbf{d}_{13} = \begin{pmatrix} 0 \\ 4.73 \\ 1.70 \end{pmatrix} \qquad \mathbf{d}_{23} = \begin{pmatrix} 4.1 \\ 2.36 \\ 1.70 \end{pmatrix}$$

The axis system was not changed between the dinuclear and trinuclear fragment and that the two Cu^{2+} ions numbered 1 and 3 are the one considered in the dinuclear calculation. Note that the extracted DMI-vector is strictly the same $\mathbf{d}_{12}^{dinuclear}$=$\mathbf{d}_{13}^{trinuclear}$ which validate the expansion to a trinuclear fragment. The three DMI vectors share the same out of plane $d_z^{ij} = 1.70K$ and in plane component $|d_{xy}^{ij}| = 4.73K$.

5.3 Conclusion

The purpose of this work was the application of *ab initio* calculation to extraction magnetic interactions in Herbertsmithite which has not been done before. The first part of the study focused on the isotropic couplings using embedded cluster method, the exploration of fragments with different sizes has been done using DFT calculations, it allowed the determination of the possible isotropic couplings. Extractions performed on the multiple fragment showed good transferability of the couplings from one cluster to the other. This justify the validity of the application of the embedded cluster method for this material. For the structure without defects, the results indicates that the only relevant in-plane coupling is between first neighbour. A reported value of $J_1 \approx 180K$ matches very well with experimental data, other couplings were found to be two order of magnitude smaller. The subject of defects was adresses as well with the study of structural deformation around the most recurring defect. The substitution of the intersite Zn^{2+} ion by a additional Cu^{2+} ion tends to modify the environment near this site due a strong Jahn-Teller effect. Two types of structure were identified, which differ by the displacement of the hidroxide groups around the intersite. As the two structure are close in energy, $\approx 100K$, the extraction of isotropic couplings was performed for both geometries. It was found that the deformations have a significant impact on the in-plane coupling, replacing the unique J_1 by two different J values. The most remarkable result of this study is the introduction of a new ferromagnetic coupling between in-plane copper ions and the intersite defect. This coupling is non negligible, $\approx 0.4|J_1|$, which could have a strong impact on the measurement at low temperature. The second part of this study focused on the extraction of anisotropic interactions on a dinuclear and trinuclear fragment. First, the extraction of the first neighbour coupling using wave-function based method was performed. It was found that an active space composed only of the d-orbitals is does not allow a good estimation of $J - 1$. To solve this problem, some orbitals of the bridging ligand were included in the active space enable following a projection procedure. Then, the Dzyaloshinskii-Moriya pseudovector and the symmetric tensor of anisotropic exchange were extracted on both fragments. A significant value of DMI was obtained with both in-plane and out-of-plane components. Results between fragment compares perfectly which validate the use of the Multi-Spin Hamiltonian to describe the anisotropy of this system.